



University of Nairobi  
Department of Physics

**Assessment of Elemental Content and Associated Radiological Exposure in  
Sand Beds of Tiva River, Kitui County**

By

George Gitau

I56/78698/2009

A Thesis Submitted in Partial Fulfilment of the Requirements for the Award of  
the Degree of Master of Science (M.Sc) in Physics, University of Nairobi

© July, 2023

## DECLARATION

This thesis is my original work and has not been submitted elsewhere for examination, award of a degree, or publication at any other University. Where other people's work or my own work has been used, this has properly been acknowledged and referenced in accordance with the University of Nairobi's requirements.

Signature  .....

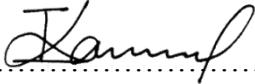
Date: ..... 25<sup>th</sup> July 2023 .....

This thesis has been submitted for examination with our approval as research supervisors:

**Dr. M. I. Kaniu**

Department of Physics

University of Nairobi

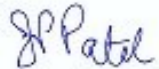
Signature  .....

Date: ..... 25<sup>th</sup> July 2023 .....

**Prof. J. P. Patel**

Department of Physics and Space Sciences

Technical University of Kenya

Signature  .....

Date: ..... 25<sup>th</sup> July 2023 .....

## ACKNOWLEDGEMENTS

First and foremost I would like to thank the Almighty God for according me the opportunity to pursue this study. It was quite a task and challenging to complete this work. The completion of this work was possible as a result of enormous support and guidance from the following persons whom I most sincerely acknowledge:

I wish to recognize, with appreciation, the distinguished support and guidance of my supervisors Dr. Ian Kaniu and Prof. J. P. Patel who dedicated their time to consultation and guidance.

In a special way, I wish to thank Prof. Eliud M. Mathu of SEKU University and the former Director of the Institute of Nuclear Science and Technology (INST), late Mr. David M. Maina who originally encouraged me at the beginning of this study.

I also wish to thank, most sincerely, the staff of INST laboratory, Messrs. Simon Bartilol and Nelson Kiprono, for their guidance during sample preparations and onward analysis with EDXRF and Gamma-ray spectroscopy.

My gratitude also goes to the Tiva area administration chief for allowing me to collect sand samples from the Tiva River. Lastly, I want to thank my family members and friends for their continued support and prayers during the course of the study.

## ABSTRACT

The geological structure of the river Tiva basin in Kitui County indicates heavy mineral sands like zircon, ilmenite, and hematite, associated with naturally occurring radioactive materials (NORM) from primordial radionuclides ( $^{40}\text{K}$ ,  $^{238}\text{U}$ , and  $^{232}\text{Th}$ ) in the grains. Natural and anthropogenic activities may raise radiation exposure levels, posing risks to both the residents and the environment. This study aimed to establish baseline radioactivity, exposure levels, and heavy metal concentrations in river Tiva sand samples. Three sections (upstream at Kauwi, midstream at Tanganyika Bridge, and downstream at Tiva Bridge) were selected. 77 samples (58 in 2017 and 19 in 2018) underwent analysis using hyperpure germanium (HPGe) gamma-ray and energy-dispersive X-ray fluorescence (EDXRF) spectrometry. A follow-up survey in 2018 assessed external gamma dose rates using a GIS-enabled portable radiation detector. The average activity concentrations in upstream, midstream, and downstream sections respectively were:  $^{238}\text{U}$  (1.5 Bq kg<sup>-1</sup>, 30 Bq kg<sup>-1</sup>, 23.5 Bq kg<sup>-1</sup>),  $^{232}\text{Th}$  (20.5 Bq kg<sup>-1</sup>, 15.5 Bq kg<sup>-1</sup>, 20 Bq kg<sup>-1</sup>),  $^{40}\text{K}$  (598 Bq kg<sup>-1</sup>, 646 Bq kg<sup>-1</sup>, 578 Bq kg<sup>-1</sup>). Compared to global averages,  $^{238}\text{U}$  and  $^{232}\text{Th}$  levels were lower, while  $^{40}\text{K}$  levels were up to 1.6 times higher. Mean gamma dose rates 1 meter above the ground were  $164\pm 36$  nGy/h,  $149\pm 42$  nGy/h, and  $124\pm 22$  nGy/h for the three sites. Elemental analysis revealed Fe (30000 $\pm$ 300ppm) and K (14700 $\pm$ 800ppm) as the richest elements, with a strong positive correlation among Fe, Mn, and Zn suggesting a common origin. Negative correlations were observed between Zr and K (-0.57), Zr and Sr (-0.65), and Zr and Rb (-0.72) indicating diverse origins. Principal component analysis explored multivariate relationships, showing a spatial distribution where Ti and Zn were more abundant upstream, while Fe was evenly distributed. The findings provide valuable reference data for radioactivity mapping and future radiological investigations, aiding the formulation of radioprotection and riverine environmental management policies.

## TABLE OF CONTENTS

DECLARATION .....	ii
ACKNOWLEDGEMENTS .....	iii
ABSTRACT .....	iv
LIST OF FIGURES .....	ix
LIST OF TABLES .....	x
LIST OF ACRONYMS & ABBREVIATIONS .....	xi
CHAPTER 1: INTRODUCTION .....	1
1.1. Background to the Study .....	1
1.2. The Geology of the Study Area.....	2
1.3. Research Hypotheses.....	4
1.3.1. Null hypothesis .....	4
1.3.2. Alternative hypothesis .....	4
1.4. Statement of the Problem .....	4
1.5. Objectives.....	5
1.5.1. Main objective .....	5
1.5.2. Specific objectives.....	5
1.6. Justification and Significance.....	6
1.7. Scope of the Research .....	7
CHAPTER 2: LITERATURE REVIEW .....	8
2.1. Heavy Mineral Sands .....	8
2.2. Characterization of Heavy Sands .....	8

2.3. Geochemistry of Radioactive Isotopes in Mineral Sands .....	11
2.4. Geochemical and Environmental Assessment of Heavy Metals in Soils.....	12
2.5. Economic Uses of Heavy Minerals .....	14
2.6. Radioactivity Measurements .....	17
2.7. Energy Dispersive X-ray Fluorescence (EDXRF) Spectrometry.....	19
2.8. Multivariate Chemometrics in EDXRF Analysis.....	21
CHAPTER 3: THEORETICAL FRAMEWORK.....	24
3.1. Introduction .....	24
3.2. The NORM Decay Series.....	24
3.3. Measurement of Potassium-40 ( $^{40}\text{K}$ ).....	26
3.4. Gamma Radiation.....	26
3.5. Theory of Gamma-Ray Spectroscopy .....	27
3.6. Activity of the Sample in Gamma-Ray Spectrometry.....	28
3.7. External Exposure to Natural Radiation from Radionuclides .....	29
3.8. Occupational Radiation Exposures .....	30
3.9. Operation Principle of EDXRF .....	30
3.10. Principal Component Analysis .....	33
CHAPTER 4: MATERIALS AND METHODS .....	34
4.1. Sampling and Sampling Locations.....	34
4.2. XRF Spectroscopy.....	36
4.2.1. Sample preparation.....	36

4.2.2. Preparation of sand samples for XRF analysis.....	36
4.2.3. Elemental analysis .....	37
4.2.4. Calculation of the elemental detection limits for XRF analysis.....	37
4.2.5. Comparison of measured results with certified values.....	38
4.2.6. Descriptive statistics of heavy metals in soils of Tiva River.....	39
4.2.7. Principle Component Analysis (PCA).....	40
4.2.8. Geospatial mapping and distribution.....	41
4.3. Gamma Ray Spectroscopy .....	41
4.3.1. Preparation of sand samples for gamma-ray analysis .....	41
4.3.2. Gamma-ray spectrometric analysis .....	42
<b>CHAPTER 5: RESULTS AND ANALYSIS .....</b>	<b>44</b>
5.1. Chapter Overview .....	44
5.2. The Average Activity Concentrations of Radionuclides in Selected Study Sections of Tiva River.....	44
5.3. External Dose Rates Distributions along Tiva River .....	46
5.4. Correlation between Dose Rate and Radioactivity Concentrations .....	50
5.5. Elemental Concentrations.....	54
5.5.1. Comparison of measured results with certified values.....	54
5.5.2. Elemental concentrations along the Tiva River.....	55
5.5.3. Principal component analysis of EDXRF measurements along Tiva River.....	62
5.5.4. Spatial distribution of heavy metal in Tiva sands .....	64
<b>CHAPTER 6: CONCLUSIONS AND RECOMMENDATIONS.....</b>	<b>67</b>

6.1. Conclusions .....	67
6.2. Recommendations and Future Work .....	68
REFERENCES .....	69
Appendices.....	78



## LIST OF FIGURES

Figure 3.1 Illustration of Gamma ray spectroscopy system .....	28
Figure 3.2 (a): $K_{\alpha}$ and $K_{\beta}$ peaks and (b):X-ray emission spectrum .....	31
Figure 3.3 Illustration of a set-up of X-ray fluorescence .....	32
Figure 4.1 Sampling sites in the upstream section of Tiva river at Kauwi Bridge .....	35
Figure 4.2 (a): sampling sites midstream and (b): sampling sites downstream .....	35
Figure 5.1 Typical gamma ray spectrum of sand sample from downstream of river Tiva.....	46
Figure 5.2 Dose distribution at (a) Kauwi bridge (upstream), (b) Tanganyika bridge (midstream) and (c) Tiva bridge (downstream) .....	47
Figure 5.3 Dose rate of environs of Tiva River .....	49
Figure 5.4 Demarcations upstream .....	51
Figure 5.5 Demarcations upstream .....	51
Figure 5.6 Correlation between radioactivity concentrations and absorbed gamma dose rates in the study area .....	53
Figure 5.7 Spectrum for sand samples obtained from Tiva river at (a) upstream, (b) midstream and (c) downstream.....	59
Figure 5.8 PCA results of Tiva river elemental data (a) Scores plot and (b) Loadings plot....	64
Figure 5.9 Downstream variation in the heavy metal and radionuclide concentrations in Tiva river.....	65
Figure 5.10 Map of the study area illustrating the terrain between the upstream and downstream sections of Tiva river .....	66

## LIST OF TABLES

Table 2.1 Minerology results of sands from the Tiva River (Kennedy, 2016) .....	10
Table 3.1 Uranium-238, Uranium-235, and Thorium-232 decay series (Gilmore, 2008).....	25
Table 3.2 Average radiation dose from natural sources (UNSCEAR, 2000) .....	29
Table 4.1 Number of samples collected from upstream, midstream and downstream .....	34
Table 5.1 Average activity concentrations (Bq kg <sup>-1</sup> ) of radionuclides .....	44
Table 5.2 Summary of average activity concentration along the river Tiva.....	45
Table 5.3 Summary of dose rate measurements along Tiva River .....	50
Table 5.4 Dose rates (nSv/h) and activity concentrations (BqKg <sup>-1</sup> ) of demarcated sites .....	52
Table 5.5 Detection limits and comparison of measured and certified values .....	54
Table 5.6 Descriptive statistics of the elements found in the upstream. (Concentrations are in ppm) .....	55
Table 5.7 Descriptive statistics of elements found in the midstream (concentrations are in ppm) .....	56
Table 5.8 Descriptive statistics of elements found in the downstream (concentrations are in ppm) .....	57
Table 5.9 EDXRF Pearson correlation analysis results .....	61
Table 5.10 Eigen values and variances for principal components measured along Tiva River .....	62

## LIST OF ACRONYMS & ABBREVIATIONS

ACRP	Association of Clinical Research Professionals
ALARA	As Low As Reasonably Achievable
ATSDR	Agency for Toxic Substances and Disease Registry
CRM	Certified Reference Material
EDXRF	Energy Dispersive X-ray Fluorescence
FA	Factor Analysis
FWHM	Full Width Half Maximum
GPS	Global Positioning System
HBRA	High Background Radiation Area
HCA	Hierarchical Cluster Analysis
HM	Heavy Metals
HPGe	High Purity Germanium
HPS	Health Physics Society
IAEA	International Atomic Energy Agency
ICRP	International Commission on Radiological Protection
INST	Institute of Nuclear Science and Technology
LOD	Limit of Detection
MCA	Multichannel Analyzer

NMBGMR	New Mexico Bureau of Geology and Mineral Resources
NORMs	Naturally Occurring Radioactive Materials
PCA	Principal Component Analysis
PLSR	Partial Least Squares Regression
REE	Rare Earth Elements
REOs	Rare Earth Oxides
UNSCEAR	United Nations Scientific Committee on the Effects of Atomic Radiation
UoN	University of Nairobi
XRD	X-ray Diffraction
XRF	X-ray Fluorescence

# CHAPTER 1: INTRODUCTION

## 1.1. Background to the Study

As individuals engage in their daily activities, they are continuously exposed to ionizing radiation present in their immediate environment. According to (UNSCEAR, 2000), the natural radioactive isotopes  $^{40}\text{K}$ ,  $^{238}\text{U}$ , and  $^{232}\text{Th}$  account for the background radiation as well as the overall radiation dose that people receive. Most materials used in building constructions such as sediments, sand, water, and quarry products among other essential building materials contain radioactivity concentrations in varying degrees. The presence of natural radionuclides in these materials leads to the emission of ionizing radiation consequently leading to external radiation exposure to people. Additionally, internal exposure occurs through the inhalation of radon,  $^{222}\text{Rn}$  from uranium, and  $^{220}\text{Rn}$  from the thorium series, which are present within building structures. Radiation protection programs have expressed significant concerns regarding the potential contact with ionizing radiation from naturally occurring radionuclide materials (NORMs).

Research shows that exposure to ionizing radiation can have multiple negative effects on humans. It not only impairs active cells but can also lead to significant health problems, such as mutations, leukemia, various types of cancer, and other illnesses (Jibiri and Okeyode, 2012; Rafique *et al.*, 2014; Taskin *et al.*, 2009). For instance, the inhalation of freely existing radon gas in the air is associated with lung cancer. Since the majority of individuals spend about 80% of their time indoors (UNSCEAR, 2000), they are consistently exposed to both external and internal radiation within the confines of buildings. (Wrixon, 2008) argues that individual radiation exposure should be kept “as low as reasonably achievable (ALARA)” in accordance with radiation protection practices. Therefore, accurately estimating the activity

and distribution of natural radionuclide concentrations in building materials and soil is crucial for assessing the level of exposure in populations and safeguarding the larger community.

Sand harvesting is a significant economic activity in Kitui County, with major sites located along rivers such as Nzeeu, Kalundu, Tiva, Mwitasyano, Mutendea, Kaayo, and Kauwi. Due to the extensive use of sand in various construction activities, researchers have conducted studies to measure radioactivity and assess radiation exposure in river residues from different locations within the county (Midigo, 2015). However, there is a dearth of research regarding the levels of radionuclide activities along the Tiva River. Consequently, this study focused on investigating the distribution of three radionuclides namely  $^{232}\text{Th}$ ,  $^{238}\text{U}$ , and  $^{40}\text{K}$  along selected sections of Tiva River in Kitui County. The research findings will contribute valuable data for environmental radioactivity monitoring initiatives undertaken by radiation protection agencies, the Ministry of Environment, Climate Change and Forestry, and health authorities in Kenya. Additionally, the results will serve as a reference guide for assessing external radiation exposure hazards, taking into account both human activities and natural events that impact radioactivity levels in Tiva River's sand sediments. Furthermore, the study will determine the concentrations of economically important heavy elements present in the sand sediments.

## **1.2. The Geology of the Study Area**

Kitui is situated within the Mozambique belt and occupies a position on a low ridge characterized by highly granitized biotite-schist and granitoid gneiss. This ridge is located at the western edge of a wide north-south range composed of alternating granitic-gneiss sheets and highly granitized metamorphic rocks. In the southern part of this belt, there is a low ridge extending from Soma Kavuta to Ndumoni, and the Tiva River runs parallel to it from Ndumoni in a southerly direction (Nyamai *et al.*, 2003; Schoeman, 1948).

One notable feature in the area is the prominent block of resilient granitoid gneisses that form the Thatha Hills. These hills stand out with their significant elevation compared to the surrounding plain. Another distinctive feature is the Yatta plateau, which acts as a dividing line between the Athi and Tiva drainage systems. The plateau owes its existence solely to a layer of coarsely porphyritic phonolite, which acts as a resilient cap overlying the Basement system. The rocks in this region can be generally classified into the Basement system and the Post Archean. These categories are further subdivided into sedimentary and intrusive rocks, which serve as sources of various minerals including hornblende, orthoclase, biotite, quartz, and microcline, among others (Githenya, 2020).

The Tiva sub-basin is located within the Mozambique belt and is characterized by a complex basement structure dominated by metamorphic rocks (Nyamai *et al.*, 2003). These rocks mainly consist of water-resistant metamorphic granulites, which typically contain red garnets, feldspars, and pyroxenes. The river channel primarily consists of mature and well-sorted sand, sometimes with minimal clay/silt content, and its subsurface pores hold water reserves. Metamorphic granulites and gneisses are the predominant components found in most river courses. Mafic granulites, rich in black heavy minerals, garnets, pyroxenes, and iron ore, have weathered to form deep red soils containing black heavy mineral sands. In certain locations, well-foliated biotite gneiss facilitates the infiltration of rainwater into the ground. The river banks are marked by white patches of sodium chloride and Kunkar limestone, which contribute to slightly salty water conditions, especially throughout low flow periods (Kitheka *et al.*, 2005).

### **1.3. Research Hypotheses**

#### **1.3.1. Null hypothesis**

There is a noteworthy difference in the levels of the Th-232, U-238, K-40, Fe, Ti, and Zr in sands sampled from different parts and depths of the Tiva River. The levels of background radiation in River Tiva are higher than the global range recommended by the ICRP.

#### **1.3.2. Alternative hypothesis**

There is a negligible difference in the levels of the Th-232, U-238, K-40, Fe, Ti, and Zr in sands sampled from different parts and depths of the Tiva River. The levels of background radiation in River Tiva are within the recommended global range.

### **1.4. Statement of the Problem**

The underlying geological structure as well as reconnaissance surveys conducted in various parts of Kitui County, particularly in the River Tiva basin, indicate the occurrence of heavy mineral sands. These studies have also revealed a correlation between heavy sands and levels of radioactivity due to the presence of primordial radionuclides in the mineral grains. However, the area has been subject to limited radiological and elemental investigations, leading to a lack of sufficient data for a comprehensive understanding of potential hazards. A recent research study aimed to characterize the heavy minerals in River Tiva sands (Kennedy, 2016), but the researcher only utilized samples collected from the middle profile at Tiva Bridge. As a result, the elemental composition of the upper and lower profiles is yet to be determined. There is, therefore, a need to carry out further investigations in the River Tiva area to evaluate the elemental concentrations and assess the radiological exposure in the region.



## **1.5. Objectives**

### **1.5.1. Main objective**

To evaluate the radiological hazards associated with the NORMs and assess elemental content in heavy metals found from sand beds of Tiva River in Kitui County.

### **1.5.2. Specific objectives**

- (i) To assess the activity concentrations of  $^{40}\text{K}$ ,  $^{238}\text{U}$ , and  $^{232}\text{Th}$  in sand samples from Tiva River.
- (ii) To evaluate the absorbed dose rates associated with sand samples in Tiva River.
- (iii) To determine the elements present in heavy minerals in sand samples from Tiva River and prepare a spatial mapping.
- (iv) To explore factors (natural and anthropogenic) affecting the distribution of heavy elements along the river.

## **1.6. Justification and Significance**

Heavy mineral sands are known to contain naturally occurring radioisotopes such as thorium-232 ( $^{232}\text{Th}$ ), uranium-238 ( $^{238}\text{U}$ ), and potassium-40 ( $^{40}\text{K}$ ). The regular harvesting of large volumes of sand from River Tiva poses a potential risk of radiation exposure to both the miners and the occupants of buildings constructed using this sand. The data obtained from this study will provide valuable insights into the extent of exposure, serving as a foundation for future investigations. The findings will also be relevant to environmental management organizations, informing residents about protection guidelines and the potential exploitation of economically significant elements, if present.

### **1.7. Scope of the Research**

This research was conducted in Tiva River, located in Kitui County. The study focused on collecting sand samples from three different bridges: Kauwi, Tanganyika, and Tiva. These collection locations were categorized as upstream, midstream, and downstream, respectively. The primary objectives of the research were to assess the radiological hazards associated with NORMs and evaluate the elemental content present in sampled sands. The study considered a depth of 0.3 m for the analysis. The research primarily centered on the analysis of  $^{40}\text{K}$ ,  $^{238}\text{U}$ ,  $^{232}\text{Th}$ , Zr, Ti, and Fe as the key elements of interest.

## **CHAPTER 2: LITERATURE REVIEW**

### **2.1. Heavy Mineral Sands**

Heavy mineral sands are mineral deposits, also known as ore deposits, characterized by a rock body containing one or more elements or minerals in quantities that hold potential economic value (Misra, 2000). These deposits can be classified into two primary categories: nonmetallic or industrial mineral deposits and metallic mineral deposits. Nonmetallic deposits consist of minerals that possess specific chemical or physical properties, including fluorite, mica, clay, garnet, asbestos, and others. Metallic deposits, on the other hand, encompass mineral deposits from which various metals such as gold, lead, copper, iron, and zinc can be extracted. Minerals within a deposit that hold economic significance are referred to as ore minerals, while the waste material is known as gangue. However, certain minerals belonging to the oxide group and sulfide group, such as ilmenite, magnetite, arsenopyrite, and pyrite, are often considered ore minerals in metallic mineral deposits, despite their actual formation as part of the gangue.

### **2.2. Characterization of Heavy Sands**

Heavy sands commonly contain minerals that are rich in iron, zirconium, and titanium. These minerals are specifically identified as ilmenite, zircon, and rutile, respectively. Various analytical techniques have been utilized to characterize heavy minerals in sands. (Reyneke and Van Der Westhuizen, 2001) employed XRF spectroscopy, scanning electron microscopy, and optical microscopy to characterize mineral sands from an Indian sand beach. Similarly, (Bouchard *et al.*, 2011) investigated the performance of XRF spectroscopy in the analysis of cement industry materials and concluded that the method was ideal for sample characterization due to its rapid and non-destructive nature. On the other hand, (Kennedy, 2016) used the EDXRF technique to analyze mineral sands from the Tiva River at

Tanganyika bridge in Kenya and employed the XRD technique to determine the structural composition of the minerals. His study revealed the presence of hematite and ilmenite minerals. The concentrations of titanium (Ti), iron (Fe), and zirconium (Zr) elements were determined as  $2.3 \pm 0.19\%$ ,  $7.3 \pm 0.6\%$ , and  $1115 \pm 136 \text{ mgkg}^{-3}$ , respectively, with higher concentrations observed downstream. This observation was attributed to the reduced hydraulic energy downstream, enabling the sedimentation of minerals. Table 2.1 shows the mineralogy results of the sands from the Tiva River.

*Table 2.1 Minerology results of sands from the Tiva River (Kennedy, 2016)*

<b>Mineral</b>	<b>Chemical formula</b>	<b>Environment</b>
Albite	$\text{NaAlSi}_3\text{O}_8$	Magmatic and pegmatitic rocks.
Hematite	$\text{Fe}_2\text{O}_3$	Magmatic, sedimentary, metamorphic, and hydrothermal.
Hornblende	$(\text{Ca, Na})_2 (\text{Mg, Fe, Al})_5 (\text{Al, Si})_8\text{O}_{22} (\text{OH})_2$	Metamorphic and igneous rocks
Ilmenite	$\text{FeTiO}_3$	Metamorphic and igneous rocks. Normally found in placers as "black sand" deposits.
Microcline	$\text{KAlSi}_3\text{O}_8$	Hydrothermal, metamorphic rocks, and granitic pegmatites.
Orthoclase	$\text{KAlSi}_3\text{O}_8$	Intrusive and extrusive igneous, and metamorphic rocks.
Quartz	$\text{SiO}_2$	Sedimentary, metamorphic, and igneous rocks.
Tremolite	$\text{Ca}_2\text{Mg}_5\text{Si}_8\text{O}_{22}(\text{OH})_2$	Contact metamorphism of Ca-rich rocks.
Diopside	$\text{CaMgSi}_2\text{O}_6$	Metamorphic rocks, and ultrabasic igneous and basic.

The data presented in Table 2.1 highlights the significant contribution of heavy minerals in coastal environments originating from igneous rocks. Among these minerals, rutile and ilmenite are the most prevalent and economically valuable heavy minerals found in heavy-mineral sands, both of which are derived from igneous rocks. (Force, 1991) provides a comprehensive analysis of igneous rocks that exhibit high enrichment in titanium dioxide ( $\text{TiO}_2$ ) and are abundant in titanium oxide minerals.

Sedimentary rocks are commonly recognized as intermediate carriers of heavy minerals found in heavy-mineral sands. They accumulate heavy minerals through the erosion of older metamorphic and igneous rocks. Sedimentary rocks, which are also referred to as "intermediate host rocks", are subjected to erosion by waves, fluvial processes, storms, and currents. Consequently, this process releases detrital heavy minerals from consolidated sedimentary rocks, leading to their remobilization and re-deposition.

The presence of titanium oxide minerals in heavy-mineral sands can be traced back to high-grade metamorphic rocks. Several studies suggest that inland complexes of high-grade metamorphic rocks contribute to the deposition of heavy minerals, particularly in coastal basins (Gosen *et al.*, 2014; Reid and Hou, 2006). While igneous rocks are often associated and mixed with metamorphic rocks, they are generally considered secondary sources of heavy minerals compared to metamorphic rocks.

### **2.3. Geochemistry of Radioactive Isotopes in Mineral Sands**

The majority of the natural radioactivity detected on Earth originates from primordial sources. Uranium is a heavy element primarily found in the Earth's crust and exhibits its activity in water, soil, and earth-based materials. It occurs naturally as  $^{238}\text{U}$  with an abundance of 99.3% (UNSCEAR, 2000). Volcanic activity is responsible for the deposition of uranium on land occurring in various rock types ranging from volcanic to sedimentary

rocks (Yu *et al.*, 2018). The concentrations of uranium can be influenced by chemical conditions and are notably present in certain substances, such as minerals like lignite, phosphate rock deposits, and uranium-rich monazite sands in ores. Geological processes and wind contribute to the continuous redistribution of uranium throughout the environment in water, rocks, and soils. Moreover, uranium is soluble in water and can be absorbed by organisms.

Natural weathering processes, including hydrodynamic processes and wind, break down rocks resulting in the incorporation of thorium and other rock components into the soil (ATSDR, 1999). Soils containing clay minerals tend to have higher thorium content (Harmsen and Haan, 1980). Living organisms require the two naturally occurring isotopes of potassium,  $^{41}\text{K}$  and  $^{39}\text{K}$ , with abundances of 6.7% and 93.3% respectively. However, the high-energy gamma radiation emitted by the primordial isotope  $^{40}\text{K}$  (0.0118%) is associated with diverse health risks (Farai *et al.*, 2006). These radionuclides and their progenies significantly contribute to the background radiation present in our surroundings. The various physicochemical states of the radionuclides affect their movement and absorption within biological systems. Uranium specifically bonds with organic substances, while thorium and potassium have a strong affinity for clays, which explains the variation in radioactivity observed when compared to other sedimentary rocks.

#### **2.4. Geochemical and Environmental Assessment of Heavy Metals in Soils**

Heavy metals are elemental components that occur naturally within the Earth's crust. However, human activities such as industrial processes, mining, and smelting have significantly increased the occurrence of heavy metals in sediments and soils worldwide. This has led to the disruption of the natural balance and altered the geochemical and biochemical cycles of particular heavy metals. As a result, the concentration of heavy metals in soils has



become a matter of great concern for environmentalists, farmers, biologists, and ecologists. Given the potential health risks associated with heavy metals and their persistence in soils, it is crucial to assess the environmental impact of soil pollution in both agricultural and non-agricultural areas. Moreover, the excessive accumulation of heavy metals in the food chain is a significant concern (Coggan *et al.*, 2008; Grzebisz *et al.*, 2001).

An environmental geochemical study has been done to evaluate the level of chemical contamination in sediment and soil within the Panzhihua region of South West China, well known for its smelting and mining activities (Teng *et al.*, 2003). The study aimed to investigate the environmental geochemistry of Pb, Cr, Ti, As, Zn, V, Cu, and Mn in soil and sediment, while also evaluating the level of pollution in the area. The study identified mining activities and the discharge of waste effluent as the primary sources of pollution for the analyzed elements. It recommended regular monitoring of trace metals, with particular emphasis on heavy metal enrichment.

In a separate study, (Otari and Dabiri, 2015) conducted a geochemical assessment to evaluate the presence of heavy metal pollution in sediments and soils of the Forumad Chromite mine located in the northeast of Iran. The study investigated the pollution of soil by heavy metals using statistical, geochemical, and environmental indicators specific to the Forumad Chromite mine. The analysis of heavy metal concentrations revealed significantly high mean levels of Ni (570.7 ppm) and Cr (5837.5 ppm) in the surrounding soils and sediments. Conversely, the measured levels of additional heavy metals, including Co, V, As, Cu, and Pb were found to be consistent with the geological background values. The environmental and geochemical assessments revealed that Co, Cr, V, and Ni shared similar properties and their presence in the soils could be attributed to the chromite deposits and ultramafic rocks in the area.

## 2.5. Economic Uses of Heavy Minerals

Geologists who specialize in heavy minerals are often fascinated by their characteristics and significance (O'Garra, 2017). These minerals hold significant economic importance on a global scale, as both metallic and non-metallic raw materials (Hresc *et al.*, 2018). Heavy minerals are traded internationally in both bagged and bulk forms. Some notable examples of heavy minerals include zircon, monazite, garnet, chromite, magnetite, staurolite, wolframite, and scheelite (Dwivedi *et al.*, 2019).

The extraction of heavy mineral sands involves the utilization of diverse tools, such as dredgers, wheel earthmovers, and bulldozers (Dwivedi *et al.*, 2019). Once extracted, the raw materials undergo further processing in the next stage. Gravity concentrators are employed initially to separate the lighter minerals (Hresc *et al.*, 2018). Subsequently, high-tension and magnetic methods are utilized to remove rutile, leucoxene, and ilmenite from the concentrate, while the remaining minerals are differentiated using techniques such as spirals, gravity tables, air tables, magnets, and high-tension magnetic separators to yield zircon (Cen *et al.*, 2021; Ghorbani *et al.*, 2017). This intricate process requires the presence of extensive plant infrastructure in close proximity (Luderer *et al.*, 2019). Different minerals hold varying economic values and are therefore separated at the plant site to mitigate the expense of transporting raw materials (Hresc *et al.*, 2018). Occasionally, residues from the extraction process are managed with the objective of land rehabilitation. Certain regions within the country are restored for agricultural purposes (Dwivedi *et al.*, 2019).

Heavy minerals are valuable resources that are essential to geologists (Ghorbani *et al.*, 2017). The process of extracting these heavy minerals has resulted in the creation of tens of thousands of jobs across various sectors involved in production and global trade, with millions of tons being traded annually (Hresc *et al.*, 2018). Employment opportunities in

different sectors have significant economic impacts as they reduce unemployment rates and contribute to a nation's gross income (Sack and Ghiorso, 2019).

Heavy minerals play a crucial role in the manufacturing of vital industrial and construction products (Dwivedi *et al.*, 2019). Their availability as raw materials provides a boost to the industrial sector, enabling manufacturing industries to produce a wide range of finished products for various purposes (Luderer *et al.*, 2019). Without some of these heavy minerals, progress in different sectors would be hindered. For instance, ilmenite and rutile are vital for the production of airplanes and snow-white colors, while zircon is essential for nuclear reactor control rods. Tantalite on the other hand is crucial for the manufacture of transistors (Kang *et al.*, 2020). Some of these heavy minerals have limited substitutes, making them more valuable and scarce. They're often concentrated in specific regions (Nong *et al.*, 2020).

Ilmenite is a substantial mineral that holds great economic significance (Dwivedi *et al.*, 2019). Its extraction does not aim to obtain titanium metal but rather to produce titanium oxide, a globally important white pigment (Hresc *et al.*, 2018). Titanium oxide has various applications in varnishes, paints, plastics, printing inks, rubbers, artificial fibers, glass, enamel, ceramics, and papers (Gauna *et al.*, 2017). The majority of extracted titanium is primarily used in the production of titanium oxide pigments (Nasdala *et al.*, 2020). The industrial processes involved in manufacturing titanium oxide pigments include the older sulfate process (Grudzien *et al.*, 2018).

Geologists also utilize heavy minerals to determine the history and origin of sedimentary rocks (Sack and Ghiorso, 2019). Since they constitute a minor part of sedimentary rocks, they need to be separated from each other to enable investigative study. The separation of these heavy minerals involves using a dense liquid in either a centrifuge or a separatory funnel (Nong *et al.*, 2020).

Zircon is used extensively in the ceramics industry when finely ground. Its exceptionally high refractive index allows for the white coloring of ceramic bodies and the opacification of melts. Consequently, zircon finds application in the manufacturing of sanitary ceramics, floor and wall tiles, industrial tiles, and glazed tiles (Gauna *et al.*, 2017). Additionally, geologists utilize zircon for geochronology purposes (Hresc *et al.*, 2018), although this application is relatively uncommon compared to others involving zircon and its chemical compounds. Zircon is also employed in the refractory industry and has diverse uses such as in nuclear fuel rods, water and air purification systems, and catalytic fuel converters (O'Garra, 2017).

In ancient history, monazite was extracted as a raw material for thorium, primarily in the form of thorium nitrate (Nasdala *et al.*, 2020). This led to the impregnation of incandescent gas mantles with thorium nitrate (Ghorbani *et al.*, 2017). Lanthanide separation was extremely challenging during that time, resulting in the accumulation of large quantities of rare earth oxides (REOs) in dumps. Small portions of REOs were used in pyrophoric alloys (Kang *et al.*, 2020). Nowadays, rare earth elements (REE) find extensive applications in various advanced technologies (Nong *et al.*, 2020). Technological advancements have also led to the development of new applications, such as the production of RE hydroxides (Grudzien *et al.*, 2018).

Sillimanite is employed in the steel industry to line smelting furnaces using different types of bricks based on the raw materials used. Examples include andalusite bricks and kyanite bricks (Krylov *et al.*, 2020). Sillimanite also finds application in the glass industry for manufacturing glass mix tanks and frameworks. Additionally, it is used in incineration plants for cement production (Zhai *et al.*, 2020).

Chromite is essential in the steel industry for producing ferrochromium, especially when ores with high magnesium content and a high chrome-iron ratio are required (Gauna *et al.*, 2017).

In the chemical industry,  $\text{Fe}_2\text{O}_3$  and  $\text{Cr}_2\text{O}_3$  are crucial for producing low-aluminum, low-silica, and low-magnesium content (Sack and Ghiorso, 2019).

Magnetite can be utilized as an additive in fertilizers, playing a vital role in the agricultural sector (O'Garra, 2017). Fertilizers aid in enhancing crop yields, which significantly contribute to the economy by generating income (Ghorbani *et al.*, 2017). Additionally, magnetite is used in the construction industry as ballast for ship-loading devices, bridges, elevators, and washing machines, thanks to its high bulkiness and density (Sack and Ghiorso, 2019). This stimulates economic growth by providing raw materials to various industries, ensuring the continuous operation of factories (Nong *et al.*, 2020). Due to its exceptional chemical and physical resistance, magnetite is also employed in physical water treatment to remove algae, turbidity, and other impurities found in water (Luderer *et al.*, 2019). This enables the production of clean water without impurities, which can be used for agricultural purposes, thereby generating income and further boosting the economy (Grudzien *et al.*, 2018).

## **2.6. Radioactivity Measurements**

Accurately quantifying naturally occurring radioactive materials in soil is highly useful. It provides essential information on radiation hazards to populations, the potential for mineral and petroleum extraction, and the geological characteristics of an area. Various techniques are employed to determine naturally occurring radioactive materials (NORMs) in geological, biological, and environmental media. These techniques include the Geiger-Muller detector and liquid scintillation. However, one of the most commonly used and powerful techniques is gamma-ray spectroscopy.

Radioactive materials typically emit gamma rays with varying intensities and energies, which can be detected and analyzed using gamma-ray spectroscopy. HPGe detector is an instrument

commonly employed for gamma-ray spectroscopy to identify and assess low levels of radioactivity in various samples. To ensure effective use, these detectors require proper calibration, which includes photo peak detection efficiency calibration and energy calibration. The former allows for quantitative assessment of radioactivity levels for individual radioisotopes, while the latter enables the identification of different isotopes based on their gamma-ray energy lines.

In a recent research study, sand samples, sediment, and soil were obtained from the coastal region near the Bay of Bengal in Potenga, Chittagong, Bangladesh (Yasmin *et al.*, 2018). The researchers used a closed-end coaxial HPGe gamma-ray detector with a resolution of 1.8 keV (FWHM) at 1332 keV of  $^{60}\text{Co}$  and a relative efficiency of 20% to evaluate the radioactivity of the samples. To determine the detection efficiency, the measured activity of the volume samples was compared to the activity of the reference samples provided by the International Atomic Energy Agency (IAEA), namely RGK-1, RGTh-1, and RGU-1. The study found that the average concentrations of the activity of  $^{232}\text{Th}$  and  $^{238}\text{U}$  followed the sequence: Sediment, Soil, and Sand. The concentrations of  $^{232}\text{Th}$  and  $^{226}\text{Ra}$  in the studied materials varied, suggesting differences in geological characteristics of the study area. Additionally, despite  $^{226}\text{Ra}$  and  $^{232}\text{Th}$  being the predominant radioactive elements in the environment, the measured activity of  $^{40}\text{K}$  exceeded their values. The average activities of  $^{40}\text{K}$ ,  $^{232}\text{Th}$ , and  $^{226}\text{Ra}$  in the analyzed samples were found to exceed the mean global values of 474 Bq/kg, 36 Bq/kg, and 33 Bq/kg respectively (UNSCEAR, 2000).

In a similar study conducted in South East Nigeria, (Isinkaye and Emelue, 2015) measured natural radioactivity and assessed radioactive risks in Lake Oguta sediments. Gamma-ray spectrometry was used to map the distribution of three naturally occurring radionuclides, namely  $^{40}\text{K}$ ,  $^{232}\text{Th}$ , and  $^{226}\text{Ra}$ , in order to evaluate radiological health concerns and cancer

risks associated with using the sediments. The study found mean activity concentrations for these radionuclides that were  $47.89 \pm 18.67$  Bq kg<sup>-1</sup>,  $55.37 \pm 32.74$  Bq kg<sup>-1</sup>, and  $1023 \pm 474$  Bq kg<sup>-1</sup> for <sup>226</sup>Ra, <sup>232</sup>Th, and <sup>40</sup>K. These values were slightly above their worldwide mean values but below the suggested limits, indicating no significant radioactive risks associated with using the sediments for construction-related purposes.

In another study, the researchers evaluated the natural radioactivity and radiation properties of a high background radiation area (HBRA) in Lambwe East, Southwestern Kenya (Achola *et al.*, 2012). They examined 21 samples using HPGe gamma-ray spectrometer and found average activity levels of 1396.85 Bqkg<sup>-1</sup>, 178.69 Bqkg<sup>-1</sup>, and 508.67 Bqkg<sup>-1</sup> for <sup>232</sup>Th, <sup>238</sup>U, and <sup>40</sup>K respectively. The outdoor measured airborne dosage rates had a mean of 2325.84 nGy h<sup>-1</sup>. Based on an assumed 0.4 occupancy factor, the obtained values corresponded to a mean annual effective dose rate of 5.705 mSv/yr, which surpassed the global average of 0.46 mSv/yr by a factor of twelve, classifying the region as an HBRA.

## **2.7. Energy Dispersive X-ray Fluorescence (EDXRF) Spectrometry**

Field-based and non-destructive techniques utilizing rapid X-ray fluorescence (XRF) have been employed to analyze multiple elements in soils for environmental assessment. However, XRF techniques are primarily used for screening purposes due to their moderate detection limits and precision, which are inadequate for accurate quantitative analysis (Strüder *et al.*, 1998). Consequently, EDXRF spectrometry was developed as a more versatile and rapid technique for quantifying soil elements. When combined with a sample pulverization procedure, the EDXRF technique has proven to be reproducible, accurate, and efficient, particularly for elements with atomic numbers greater than 13. The EDXRF technique relies on the interaction between X-rays and a sample, where the distinctive atomic structure of

each element produces discernible peaks on its X-ray emission spectrum, enabling effective characterization.

(Jørgensen *et al.*, 2005) conducted a research study in Copenhagen whereby polluted soil from a former horticultural land, now a recreational area, was analyzed using multi-elemental EDXRF mapping. The land had been treated with pesticides containing toxic elements during its horticultural production period, potentially leading to a significant accumulation of toxic elements in the topsoil. Since heavy metals and toxic elements persist in soils for extended periods, high concentrations typically become evident several years after their application. Therefore, assessing these toxic elements and heavy metals is crucial for guiding present and future land utilization decisions. The selection of the study site was based on the suspicion that the land could be contaminated with hazardous substances that could harm the current users of the recreational area. After analysis of soil samples using EDXRF, the topsoil across the entire site exhibited relatively stable concentration levels for majority of the elements. However, the hazardous components, namely Pb, Cu, As, and Zn, exhibited significant variation within the area. Samples with elevated levels of As indicated the previous application of pesticides containing toxic elements on the topsoil of the former horticultural land. Furthermore, the enrichment of As, Cu, and Zn was highest in the top 20 cm of the soil, and these elements were not enriched through anthropogenic means below a depth of 50 cm, suggesting their inert behavior in the examined soil. The investigation results highlight the usefulness of combining EDXRF with multivariate statistics for conducting multi-element mapping, as well as understanding the sources and mobility of the land.

In another study, (Adebiyi and Ore, 2021) utilized EDXRF spectrometry to assess the presence of toxic or harmful substances in the tailings of oil sands in Nigeria. The study focused on detecting and measuring the concentrations of 17 elements, namely V, As, Ti, Sc,



K, Zr, Ga, Nb, Mn, Cu, Sr, Fe, Zn, Ca, Se, Rb, and Ni. The results indicated that As had the lowest concentration, ranging from 66 to 101  $\mu\text{g/g}$  (mean:  $81.75 \pm 17.91 \mu\text{g/g}$ ), while Fe exhibited the highest concentration range of 8159 to 11,581  $\mu\text{g/g}$  (mean:  $9453 \pm 1477.72 \mu\text{g/g}$ ). Furthermore, the elemental concentrations surpassed those found in bitumen and Nigerian oil sands, suggesting that a significant proportion of these elements had been extracted into the tailings, including the water disposed of as waste during the bitumen collection process from the oil sands. The study also revealed strong inter-elemental clustering among the elements, namely V, Ti, Sr, Mn, Cu, Zr, Ga, K, Ni, As, Nb, Zn, V, Ca, and Sc, indicating a chemical affinity and potentially similar origins. If the tailings are improperly disposed of, the elevated levels of these elements pose risks not only to human health but also contribute to environmental degradation after prolonged exposure.

(Nzuki, 2017) aimed to assess the presence of heavy metals in the soils of Block C in the Mui Basin in Kitui County, Kenya. The study involved the collection of forty randomly sampled soil samples from Block C, which were then analyzed for heavy metal content using EDXRF technique. The EDXRF analysis of the soil samples indicated average concentrations of 52657 mg/kg for iron, 355 mg/kg for vanadium, 89 mg/kg for zinc, 1637 mg/kg for manganese, 45 mg/kg for copper, 423 mg/kg for strontium, and 30 mg/kg for lead. It was observed that elevated concentrations were found in samples collected from regions with significant human practices, including farming, market areas, and sand harvesting.

## **2.8. Multivariate Chemometrics in EDXRF Analysis**

In order to address the limitations of the classical EDXRF technique discussed in section 2.6, various multivariate chemometric techniques such as factor analysis (FA), hierarchical cluster analysis (HCA), regression, and principal component analysis (PCA) have been employed for analyzing XRF spectra for both multivariate calibration and pattern recognition. Among these

techniques, PCA is widely used and was utilized in this study. It is a method that reduces the dimensionality of large datasets while minimizing information loss and enhancing interpretability. It achieves this by creating uncorrelated new variables that maximize variance. PCA is commonly employed to accurately determine and interpret the relationships between variables.

In an environmental and geochemical study conducted to assess heavy metals in sediments and soils of the Forumad Chromite mine in northeastern Iran, 12 elements including K, Fe, As, Cu, V, Ni, Na, Cd, Mo, Co, Pb, and Cr were identified (Otari and Dabiri, 2015). A four-component PCA model was applied to the collected data. The first component consisted of Cr, Ni, V, Co, and Fe, while the second component included Mo, Cd, Na, and K. The third component correlated Cu and As. Pb was relatively independent but had a slight dependence on the first component. Multivariate analysis, specifically Pearson's correlation, revealed a strong positive correlation between Cr and V ( $r = 0.932$ ,  $p < 0.01$ ), Co ( $r = 0.824$ ,  $p < 0.01$ ), and Ni ( $r = 0.770$ ,  $p < 0.01$ ), indicating a shared origin.

(Büchele *et al.*, 2019) analyzed a diverse soil set comprising 598 samples from 12 distinct study regions in Germany using EDXRF. Initially, PCA was conducted to identify any similarities within the set of samples. The four textural classes (sand, silt, clay, and loam) exhibited observable clustering patterns due to variations in iron composition ratios. The capability of univariate and multivariate data analysis utilizing partial least squares regression (PLSR) was explored to accurately determine the nutrients in German agricultural samples. Iron and potassium were the preferred nutrients in the performance test of the two calibration sample sets. The estimation of iron and potassium in all soil samples prepared using EDXRF exhibited higher accuracy levels with PLSR, as indicated by the improved overall average deviation. This justifies the selection of PLSR for data evaluation.



## CHAPTER 3: THEORETICAL FRAMEWORK

### 3.1. Introduction

Materials of environmental origin, such as soil and water, are assessed for two main purposes: to establish background radiation levels and to evaluate contamination levels resulting from natural causes or human activities. Gamma spectrometry is commonly used to measure cosmogenic nuclides such as  $^{232}\text{Th}$ ,  $^{40}\text{K}$ ,  $^{235}\text{U}$ , and  $^{238}\text{U}$ . These nuclides are accompanied by daughter nuclides of uranium and  $^{232}\text{Th}$  isotopes. Naturally occurring radioactive materials (NORMs) is the term used to refer to naturally occurring substances that contain these radioactive elements (Gilmore, 2008). Successful gamma spectrometry of samples that contain these radionuclides requires a comprehensive understanding of their decay chains.

### 3.2. The NORM Decay Series

Thorium and uranium are considered unstable elements primarily because they undergo alpha-particle emission, resulting in the formation of radioactive nuclides. Natural uranium comprises three isotopes:  $^{238}\text{U}$ , a lesser percentage of  $^{235}\text{U}$ , and  $^{234}\text{U}$ , which is a decay-series daughter of  $^{238}\text{U}$ . On the other hand, natural thorium consists of a single isotope,  $^{232}\text{Th}$ . As these nuclides decay, a series of successive nuclides are produced, eventually leading to the stable isotopes of lead. Table 3.1 shows the three decay series.

Table 3.1 Uranium-238, Uranium-235, and Thorium-232 decay series (Gilmore, 2008)

Uranium 238 series	Uranium 235 series	Thorium 232 series
1. $^{238}\text{U}$ $4.468 \times 10^9$ y	1. $^{235}\text{U}$ $7.04 \times 10^8$ y	1. $^{232}\text{Th}$ $1.405 \times 10^{10}$ y
$\downarrow\alpha$	$\downarrow\alpha$	$\downarrow\alpha$
2. $^{234}\text{Th}$ 24.10 d	2. $^{231}\text{Th}$ 25.52 h	2. $^{228}\text{Ra}$ 5.75 y
$\downarrow\beta$ $\downarrow\beta$	$\downarrow\beta$	$\downarrow\beta$
3. $^{234\text{m}}\text{Pa}$ 1.17 m $\downarrow\text{IT}$	3. $^{231}\text{Pa}$ $3.276 \times 10^4$ y	3. $^{228}\text{Ac}$ 6.15 h
$^{234}\text{Pa}$ 6.70 h	$\downarrow\alpha$	$\downarrow\beta$
$\downarrow\beta$ $\downarrow\beta$	4. $^{227}\text{Ac}$ 21.772 y	4. $^{228}\text{Th}$ 1.9127 y
4. $^{234}\text{U}$ $2.455 \times 10^5$ y	$\downarrow\beta$	$\downarrow\alpha$
$\downarrow\alpha$	5. $^{227}\text{Th}$ 18.718 d	5. $^{224}\text{Ra}$ 3.627 d
5. $^{230}\text{Th}$ $7.538 \times 10^4$ y	$\downarrow\alpha$	$\downarrow\alpha$
$\downarrow\alpha$	6. $^{223}\text{Ra}$ 11.43 d	6. $^{220}\text{Rn}$ 55.8 s
6. $^{226}\text{Ra}$ 1600 y	$\downarrow\alpha$	$\downarrow\alpha$
$\downarrow\alpha$	7. $^{219}\text{Rn}$ 3.96 s	7. $^{216}\text{Po}$ 150 ms
7. $^{222}\text{Rn}$ 3.8232 d	$\downarrow\alpha$	$\downarrow\alpha$
$\downarrow\alpha$	8. $^{215}\text{Po}$ 1.781 ms	8. $^{212}\text{Pb}$ 10.64 h
8. $^{218}\text{Po}$ 3.094 m	$\downarrow\alpha$	$\downarrow\beta$
$\downarrow\alpha$	9. $^{211}\text{Pb}$ 36.1 m	9. $^{212}\text{Bi}$ 60.54 m
9. $^{214}\text{Pb}$ 26.8 m	$\downarrow\beta$	$\downarrow\beta$ $\downarrow\alpha$
$\downarrow\beta$	10. $^{211}\text{Bi}$ 2.14 m	10. $^{212}\text{Po}$ 0.300 $\mu\text{s}$
10. $^{214}\text{Bi}$ 19.9 m	$\downarrow\alpha$	$\downarrow\alpha$
$\downarrow\beta$	11. $^{207}\text{Tl}$ 4.77 m	11. $^{208}\text{Tl}$ 3.060 m
11. $^{214}\text{Po}$ 162.3 $\mu\text{s}$	$\downarrow\beta$	$\downarrow\beta$
$\downarrow\alpha$	<b>STABLE <math>^{207}\text{Pb}</math></b>	<b>STABLE <math>^{208}\text{Pb}</math></b>
12. $^{210}\text{Pb}$ 22.3 y		
$\downarrow\beta$		
13. $^{210}\text{Bi}$ 5.013 d		
$\downarrow\beta$		
14. $^{210}\text{Po}$ 138.4 d		
$\downarrow\alpha$		
<b>STABLE <math>^{206}\text{Pb}</math></b>		

### 3.3. Measurement of Potassium-40 ( $^{40}\text{K}$ )

In nature, potassium exists in three isotopes:  $^{39}\text{K}$  (93.3%),  $^{41}\text{K}$  (6.7%), and  $^{40}\text{K}$  (0.0117%). The isotope  $^{40}\text{K}$  is unstable and undergoes beta decay. Specifically, potassium-40 ( $^{40}\text{K}$ ) is a radioisotope of potassium with a prolonged half-life of  $1.251 \times 10^9$  years. It constitutes 0.012% (120 ppm) of the total naturally occurring potassium. This isotope is the primary contributor to our background radiation. Interestingly,  $^{40}\text{K}$  is an uncommon isotope that can undergo all three forms of beta decay. In approximately 89.28% of cases, it disintegrates to calcium-40 ( $^{40}\text{Ca}$ ), resulting in the emission of an electron with an associated energy of 1.33 MeV and an accompanying antineutrino. Around 10.72% of the time, it disintegrates to argon-40 ( $^{40}\text{Ar}$ ) through electron capture, accompanied by the production of a neutrino and a 1460 KeV gamma ray (Wang *et al.*, 2021).

### 3.4. Gamma Radiation

Gamma rays, also referred to as gamma radiation ( $\gamma$ ), are a penetrating form of electromagnetic radiation that arises when atomic nuclei undergo radioactive decay. Gamma radiation possesses the highest photon energy due to its composition of electromagnetic waves characterized by the shortest wavelengths. Gamma rays produced through radioactive decay generally fall within the range of a few KeV to approximately 8 MeV, corresponding to the average energy levels found in nuclei with relatively long lifetimes. Consequently, gamma spectroscopy can be employed in the identification of decaying radionuclides by analyzing their energy spectrum.

### 3.5. Theory of Gamma-Ray Spectroscopy

Gamma spectroscopy provides a non-destructive, convenient, and direct method for quantifying the radioactivity content of various radionuclides in environmental samples based on their characteristic gamma energy lines. Gamma rays emitted by radioactive sources exhibit a range of energies and intensities. These emissions are detected and analyzed using a spectrometer resulting in the generation of an energy spectrum. The specific spectrum is determined by the gamma-emitting nuclides present in a given source. According to (Knoll, 1997), during analysis, the sample under examination is placed on the HPGe detector, and when the nuclides present in the sample come into contact with the detector crystal, one of the three primary processes occurs: Pair Production, the Compton Effect, or the Photoelectric Effect. Each successful interaction deposits energy and generates electron pairs, resulting in electron-hole pairs within the detector. The resulting electric charge quantity and the energy of the incident photon are directly related. The electric charge (electron-hole pairs) is converted into pulses and observed as peaks (pulse height) within the detector's active volume. These pulses provide information about the type of radiation being detected. Figure 3.1 illustrates a gamma ray spectroscopy system. A multichannel analyzer (MCA) is employed to analyze the voltage pulses generated for each gamma ray that interacts within the detector volume. Finally, the output from the MCA is sent to a computer for data analysis and display.

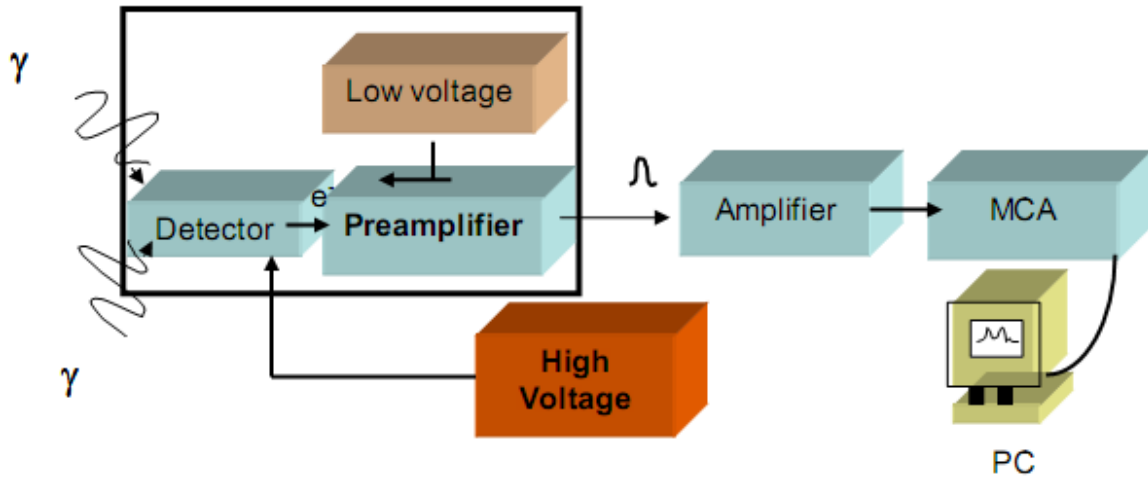


Figure 3.1 Illustration of Gamma ray spectroscopy system

### 3.6. Activity of the Sample in Gamma-Ray Spectrometry

The equation below is used to calculate the activity of a sample in gamma spectrometry;

$$A_s = \frac{I_s}{E_x M_s P_r} \dots\dots\dots 3.1$$

Where  $A_s$  is the sample activity,  $E_x$  is the reference standards efficiency,  $M_s$  is the sample mass,  $I_s$  is the sample intensity and  $P_r$  is the emission probability.

The active concentrations in Bq kg<sup>-1</sup> for all samples are determined by calculating the area under the spectrum. There were three significant gamma lines for each sample: <sup>212</sup>Pb line from <sup>232</sup>Th, <sup>40</sup>K peak, and <sup>214</sup>Pb line from <sup>238</sup>U. The activity of <sup>40</sup>K was assessed from the 1459.91 KeV peak of <sup>228</sup>Ac, <sup>238</sup>U from the 351 keV gamma line of <sup>214</sup>Pb, and the activity of <sup>232</sup>Th from the 238 keV gamma line of <sup>212</sup>Pb.



### 3.7. External Exposure to Natural Radiation from Radionuclides

Ionizing radiation originating from natural sources is an inherent aspect of life on Earth. Natural background radiation is responsible for the highest percentage of human exposure, with the global mean annual effective dose per person being 2.4 mSv. The primary sources of exposure are naturally occurring radionuclides, including  $^{238}\text{U}$ ,  $^{40}\text{K}$ , and  $^{232}\text{Th}$  (Mohanty *et al.*, 2004). Among these radionuclides, K-40 is abundantly found in nature and can be detected in rocks, rivers, sand, soils, and mineral ores, among other locations. This radioisotope (K-40) is also present in the decayed remains of plant and animal organisms. As rocks undergo weathering and erosion, K-40 can migrate and enter food chains, thereby potentially impacting human health (Shah *et al.*, 2008). Consequently, considering the potential health hazards associated with human exposure to radioactivity, it is essential to estimate the activity concentration in environmental samples. Table 3.2 illustrates the mean doses of radiation from natural sources.

Table 3.2 Average radiation dose from natural sources (UNSCEAR, 2000)

	Source	Worldwide average annual effective dose (mSv)	Typical range(mSv)
<b>External exposure</b>	Cosmic radiation	0.4	0.3 -1.0
	Terrestrial gamma rays	0.5	0.3 - 0.6
<b>Internal exposure</b>	Inhalation (mainly radon)	1.2	0.2-1.0
	Ingestion	0.3	0.2 -0.8
<b>Total</b>		2.4	1-1.0

### **3.8. Occupational Radiation Exposures**

Certain occupations, such as mining, medical clinical work, and nuclear installation work, expose workers to radiation from man-made sources. However, some workers face high levels of radiation exposure from natural sources. The term "occupational hazard" refers to the risks, both short-term and long-term, that can arise from the workplace environment. This concept falls within the field of occupational safety and public health. Long-term risks associated with occupational hazards include an increased potential for developing heart disease or cancer, while physical injuries are among the short-term risks that can be encountered.

### **3.9. Operation Principle of EDXRF**

In EDXRF spectroscopy, an atom is bombarded with an energetic beam of primary X-rays. To generate X-rays, a metal target is typically bombarded with fast electrons that have been accelerated by a high voltage. When the bombarding electrons have sufficient energy, electrons from the inner shells of the metal atoms are expelled to the outer shells. An electron is considered to be in an excited and unstable state when it occupies an energy shell higher than its ground state. In such a case, the electron undergoes de-excitation and transitions to a lower orbital. During this de-excitation process, characteristic X-rays, also known as fluorescence, are emitted, which are specific to each element and appear as spectral lines. The associated wavelength and energy of the emitted photon correspond to the difference in binding energies between the two orbitals. When vacancies occur in the K-shell ( $n=1$ ) of an atom and electrons from excited states fill these vacancies, the characteristic X-ray emission produces distinct peaks as seen in Figure 3.2 (a). The  $K_{\alpha}$  lines represent transitions from the  $n=2$  to  $n=1$  levels, while the  $K_{\beta}$  lines represent transitions from the  $n=3$  to  $n=1$  levels.

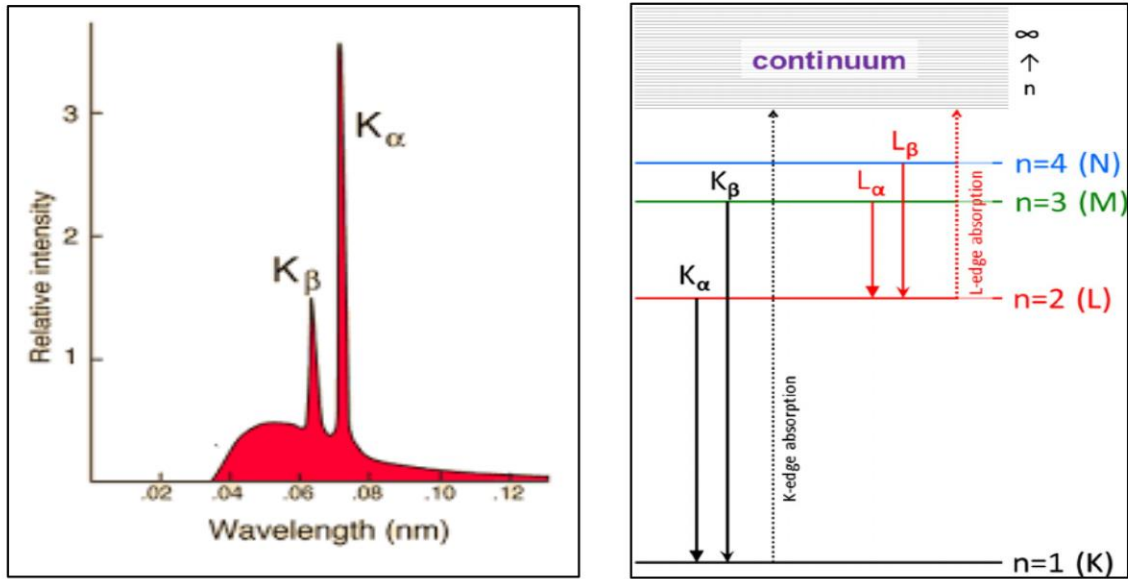


Figure 3.2 (a):  $K_\alpha$  and  $K_\beta$  peaks and (b): X-ray emission spectrum

The count rate of different elemental peaks can be determined by analyzing the energy of the X-ray peaks in a sample's spectrum. This allows for a qualitative determination of the elemental composition of the samples and subsequently enables the quantitative measurement of element concentrations. The elemental concentration was determined using the equation below for the fluorescence intensity ( $I$ ) of element  $i$  (IAEA, 2005).

$$I_i = S_i c_i (\rho d) \left[ \frac{1 - e^{-(\mu d)}}{(\mu d)} \right] \dots\dots\dots 3.2$$

Where the term in brackets is the absorption correction factor,  $c_i$  is the elemental constant and  $a$  is the absorption coefficient for the primary and fluorescent X-ray in the model.

The spectroscopy provides a measurement of the intensity of fluorescent X-rays in counts per second, represented as a fraction. Figure 3.3 shows an illustration of the spectroscopy.

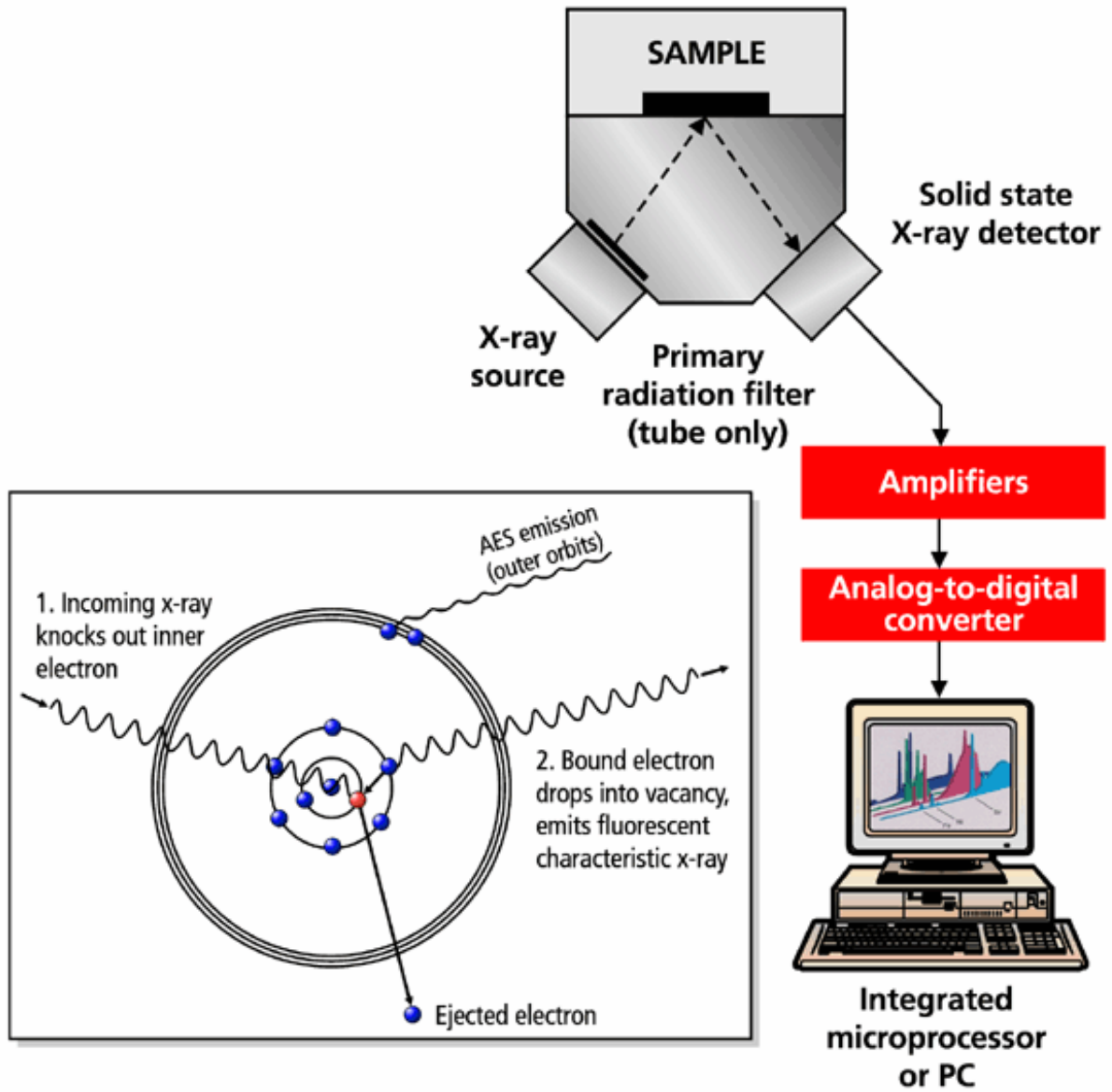


Figure 3.3 Illustration of a set-up of X-ray fluorescence

### **3.10. Principal Component Analysis**

Principal Component Analysis (PCA) was used in this research. PCA is a statistical technique used to describe large datasets in a lower-dimensional space, allowing for data reduction by identifying a smaller number of principal components or independent factors. This enables the analysis of relationships among the observed variables. The process begins with the construction of a correlation matrix that elucidates the dispersion of the initial variables, followed by the extraction of eigenvalues and eigenvectors. Through PCA, associated variables are minimized, resulting in a reduced set of orthogonal factors that effectively capture the correlations among the initial variables. This simplifies the interpretation of a multidimensional system by revealing the underlying relationships.

## CHAPTER 4: MATERIALS AND METHODS

### 4.1. Sampling and Sampling Locations

A total of 73 samples were acquired from three different sections of the Tiva River: 21 samples from Kauwi (Upstream), 19 samples from Tanganyika (Midstream), and 18 samples from Tiva Bridge (Downstream). Each sample was packed into polythene bags and properly labeled with sample identification numbers corresponding to the respective river sections. The approximate weight of each sample was 0.5kg. GPS was used to record the precise locations of the individual samples. Table 4.1 below provides a breakdown of the number of samples acquired from each section.

*Table 4.1 Number of samples collected from upstream, midstream and downstream*

<b>Sample site location</b>	<b>Section of Tiva River</b>	<b>No of samples</b>	<b>Sample codes</b>
Kauwi	Upstream	20	C1 - C18, 9a, 9b
Tanganyika	Midstream	13	a, b, c
Tiva bridge	Downstream	40	A1-A21, B1-B19

For each sampling location, one sample was collected approximately 1m from each side of the river bank, and another sample was taken from the middle of the river. This formed a set of three samples in a line. The same sampling approach was repeated at intervals of 50m to form subsequent sets. These sets were taken on both sides of each bridge. A summary of the sampling approach and locations can be found in the table provided in the appendix.

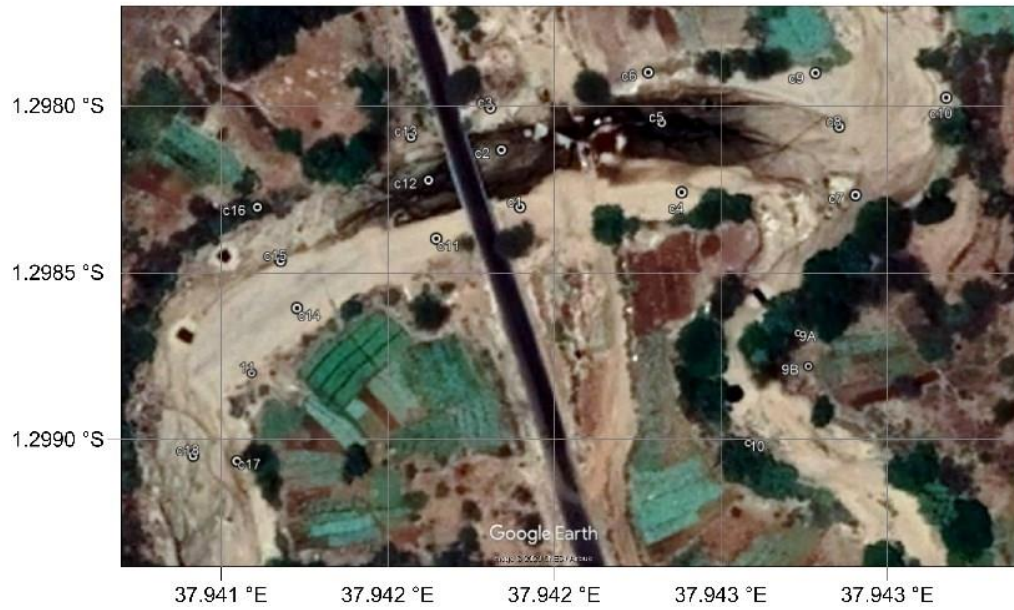


Figure 4.1 Sampling sites in the upstream section of Tiva river at Kauwi Bridge



Figure 4.2 (a): sampling sites midstream and (b): sampling sites downstream

## **4.2. XRF Spectroscopy**

### **4.2.1. Sample preparation**

Sample preparation involves several steps, including drying, crushing, and sieving, in order to obtain the most suitable form of the sample for measuring its elements and radioactivity. These steps not only ensure the preservation of the sample but also contribute to achieving a more homogeneous state.

### **4.2.2. Preparation of sand samples for XRF analysis**

For elemental analyses using EDXRF, the samples underwent a series of preparation steps. Firstly, the samples were air dried for a duration of two weeks by spreading them on individual sheets of paper in a closed room with an estimated temperature of 25 °C. To further reduce moisture content, the samples were subsequently oven-dried for eight hours at approximately 40 °C. Following drying, the samples were pulverized using an electronic pestle and mortar to achieve size reduction and homogeneity.

After pulverization, the samples were sieved using a sieve with a pore diameter of 75 µm, resulting in grains of the desired size. To aid particle binding, approximately 0.7 grams of the refined sample was mixed thoroughly with approximately 0.3 grams of starch. From each sample, three pellets weighing around 0.4 grams each were prepared using a hydraulic pellet press, making them ready for EDXRF analysis. To ensure cleanliness and prevent contamination, the pellets were carefully labeled and placed on a petri dish for further handling and analysis.



### 4.2.3. Elemental analysis

The samples were analyzed using the Amptek-EDXRF spectrometer at the Institute of Nuclear Science and Technology (INST) at the University of Nairobi (UoN). The spectrometer employed an X-ray tube equipped with a silver target and a Si-Li detector. The energy settings were configured to 30 KeV with a current of 80  $\mu$ A. The sample pellets were irradiated for a duration of 200 seconds to generate a spectrum. The sample target for matrix correction was irradiated separately for 50 seconds, and subsequently, the sample combined with the sample target was scanned for an additional 50 seconds. AXIL (Analysis of X-ray spectra by Iterative Least-squares fitting) software provided by the IAEA was used to perform spectral de-convolution and quantification of the sample. The resulting data was then presented as the mean elemental concentration for all the samples analyzed.

### 4.2.4. Calculation of the elemental detection limits for XRF analysis

The lowest quantity of a substance that can be distinguished from the absence of that particular substance or simply from a blank value is referred to as the limit of detection (LOD). The lower limit of detection values for solid samples prepared in pellet form was also determined from the evaluation of PTXRFIAEA-09 River clay. The equation below was used to calculate these values.

$$DL = \frac{3C\sqrt{N_B}}{N_P} \dots\dots\dots 4.1$$

where

C represents the concentration of the element (ppm)

$N_P$  represents the net peak area for the element, and

$N_B$  represents the net background area under the element peak

#### 4.2.5. Comparison of measured results with certified values

The validation of measurement procedures is among the most common uses of certified reference materials (CRM). This is achieved by performing measurements on certified reference materials and the outcomes evaluated against recognized values. This method takes into account the measured value, the certified value, and their corresponding uncertainties. Finally, these uncertainties are added, and the increased uncertainty is contrasted with the variance. The variation between the average measured value and the certified value can be computed after the measurement of a CRM as follows:

$$\Delta_m = |C_m - C_{CRM}| \dots\dots\dots 4.2$$

where

$\Delta_m$  is the absolute difference between mean measured value and certified value

$C_m$  is the mean measured value

$C_{CRM}$  is the certified value

The individual measurements have an uncertainty  $u_m$  meaning that any measurement outcome is discernible within this uncertainty's bounds. Similarly, a CRM's certified value can only be accepted with the defined uncertainty  $u_{CRM}$  noted on the certificate. Even though standard deviations are the most common way to convey uncertainty, only the variances given by the squared standard deviations are cumulative. The uncertainty of  $\Delta_m$  is  $U_\Delta$ , which is computed from the uncertainty of the measurement result and the uncertainty of the certified value in accordance with:

$$u_\Delta = \sqrt{u_m^2 + u_{CRM}^2} \dots\dots\dots 4.3$$

$u_\Delta$  is the combined uncertainty of result and certified value (= uncertainty of  $\Delta_m$ )

$u_m$  is the uncertainty of the measurement result

$u_{CRM}$  is uncertainty of the certified value

The expanded uncertainty  $U_\Delta$ , which corresponds to a confidence level of around 95 %, is determined by multiplying  $u_\Delta$  by the coverage factor ( $k$ ), represented by the value 2.

$$U_\Delta = 2u_\Delta \dots\dots\dots 4.4$$

Where  $U_\Delta$  is the expanded uncertainty of variance between result and certified value.  $\Delta_m$  is compared with  $U_\Delta$  to evaluate method performance; the certified value and the measured outcome are identical, and there is no discernible difference if  $\Delta_m$  is less or equal to  $U_\Delta$ .

#### **4.2.6. Descriptive statistics of heavy metals in soils of Tiva River**

Standard statistical analysis, including kurtosis, skewness, standard deviation, and mean, was performed to characterize the heavy metal contents in the soil. Kurtosis measures the extent to which scores cluster in the tails or peaks of a frequency distribution. For a univariate normal distribution, the kurtosis value is typically 3. When the kurtosis exceeds 3, it indicates heavier tails compared to a normal distribution. Skewness quantifies the asymmetry or distortion in a symmetrical bell curve or normal distribution. If the curve is shifted to the right or left, it is considered skewed. Additionally, Pearson's correlation analysis was applied to investigate whether there is a significant relationship between the heavy metal concentrations in diverse soil samples.

#### **4.2.7. Principle Component Analysis (PCA)**

The procedures followed for PCA were as follows. First is the standardization; to guarantee that each variable contributes equally to the study, this phase seeks to normalize the range of the continuous beginning variables. This is followed by covariance matrix computation; which helps to comprehend the variance from the mean of the variables of the input data set with respect to each other. In other words, it helps to identify any relationship between the variables. To address the possibility of variables being highly correlated to the extent that they contain redundant information, the covariance matrix is calculated. The eigenvalues and eigenvectors of the covariance matrix are calculated to determine the principal component. The highest conceivable variance in the data set is accounted for by the first main component. The next highest variation is explained by the second principal component, and so on. Next, the feature vector is determined by identifying the principal components based on their significance. The decision is made whether to retain all components or discard those with low significance (low eigenvalues), resulting in the formation of a matrix of vectors known as the Feature Vector containing the remaining components. Finally, the data is transformed along the axes of the principal components. The objective is to realign the data from its original axes to the ones characterized by the principal components, hence the name Principal Components Analysis. This transformation is achieved by utilizing the feature vector generated from the eigenvectors of the covariance matrix. A scree plot is then obtained showing percentages of variance by each principal component.

#### **4.2.8. Geospatial mapping and distribution**

Geospatial method was used to understand the location of the contaminants in addition to providing a comprehensive picture of the spatial distribution of the contaminants across a wider region (Nobi *et al.*, 2010). In the current study, the dispersion pattern of heavy metals was shown using the kriging technique and MapInfo software (version 8.5). The distribution of heavy metals represented as contour maps demonstrates the regional variance in metal concentrations in the three sites of study namely; upstream, midstream and downstream of Tiva River. In addition, the study assessed the likely sources of enrichment and identified areas of high metal concentrations from sand samples collected in different sections of Tiva River.

### **4.3. Gamma Ray Spectroscopy**

#### **4.3.1. Preparation of sand samples for gamma-ray analysis**

A HPGe Gamma-ray detector was utilized to measure the concentrations of  $^{232}\text{Th}$ ,  $^{238}\text{U}$ , and  $^{40}\text{K}$  in the pulverized sand samples. About 300 g of the electronic pestle and mortar-pulverized samples were packed in 250 ml plastic containers for a month prior to analysis. This allowed the gaseous  $^{222}\text{Rn}$  with a half-life 3.8 days, together with its two short-lived decay daughters, namely  $^{214}\text{Pb}$  and  $^{214}\text{Bi}$ , to reach secular equilibrium with the long-lived  $^{226}\text{Ra}$  precursor within the sample (Scott *et al.*, 1992).

### 4.3.2. Gamma-ray spectrometric analysis

Multi-nuclide reference materials were analyzed every morning for the energy calibration using the  $^{137}\text{Cs}$  line at 661.67 keV while the resolution of the system was assessed using  $^{60}\text{Co}$  at 1332.5 keV to check the stability of the HPGe system. Each sample was then placed into a sample holder in a shielded detector and measured for 12 hours. The identical test settings were applied using an empty container to quantify the environmental gamma background radiation prior to the sample measurement. Later, the obtained gamma-ray spectra were subtracted from the background observations of the individual samples as a corrective measure for the net peak areas for the counts. For quantification purposes and quality control of the HPGe, IAEA reference materials were used i.e RGK-1 for  $^{40}\text{K}$ , RGTh-1 for  $^{232}\text{Th}$ , RGU-1 for  $^{238}\text{U}$ , and mixed Soil SRM. To determine the various radionuclides' activity concentrations in Bq/kg, the absolute method was adopted using the results obtained from the samples and those from certified reference materials. This was actualized by obtaining the reference materials' efficiencies from the efficiency calibration curve and using equation 4.5 to compute the activity concentrations.

$$A_s = \frac{I_s}{E_x M_s P_r} \dots\dots\dots 4.5$$

Where

$A_s$  is the sample activity

$E_x$  is the reference standards efficiency

$M_s$  is the sample mass

$I_s$  is the sample intensity

$P_r$  is the emission probability

The active concentrations (in Bq kg<sup>-1</sup>) in all the samples were calculated using the area under the spectral peaks. There were three major gamma lines for each sample: the <sup>212</sup>Pb line from <sup>232</sup>Th, the <sup>40</sup>K peak, and the <sup>214</sup>Pb line from <sup>238</sup>U. From the 1459.91 KeV peak of <sup>228</sup>Ac the activity of <sup>40</sup>K was assessed while the activity <sup>238</sup>U from 351 KeV gamma line of <sup>214</sup>Pb and that of <sup>232</sup>Th from 238 KeV gamma line of <sup>212</sup>Pb.

## CHAPTER 5: RESULTS AND ANALYSIS

### 5.1. Chapter Overview

This chapter outlines the results obtained from the analysis of data collected from three selected study areas: Kauwi bridge on Thika-Kitui road (Upstream), Tanganyika Bridge (Midstream) on Machakos Kitui road, and Tiva Bridge on Tiva road (downstream). The results are followed by a discussion based on these findings.

### 5.2. The Average Activity Concentrations of Radionuclides in Selected Study

#### Sections of Tiva River

The Table 5.1 below shows the average activity concentrations of natural nuclides  $^{232}\text{Th}$ ,  $^{238}\text{U}$  and  $^{40}\text{K}$  from the three sections of Tiva River. The activities include the lower and upper part of each bridge.

*Table 5.1 Average activity concentrations (Bq kg-1) of radionuclides*

Location		Along the left bridge (Bq kg-1)			In the middle (Bq kg- 1)			Along the right bridge (Bq kg-1)		
		Th-232	U-238	K-40	Th-232	U-238	K-40	Th-232	U-238	K-40
<b>Upstream</b>	upper	22	23	705	20	28	603	17	30	565
	lower	30	33	616	17	40	554	14	22	546
	mean	26	28	661	18	34	579	15	26	555
<b>Midstream</b>	upper	7	8	697	16	8	409	32	15	793
	lower	9	8	660	8	6	850	14	11	587
	mean	8	8	679	12	7	630	23	13	690
<b>Downstream</b>	upper	23	36	491	23	42	481	22	36	621
	lower	19	20	668	16	23	599	18	21	609
	mean	21	28	579	19	32	540	20	28	615



It was noted that the activities of the radionuclides were higher downstream than either mid or upstream. However, in the midstream the activity concentrations were relatively lower with some of the samples having Th-232 below detection limits, see Table X in the Appendix. The high radioactivity levels of K-40 (world average 400Bq kg-1) is an indication of the presence of minerals such as monazite, ilmenite which are composed of elements associated with radioactivity in the sand samples collected. An anomaly was noted with sample A19 whose concentrations of <sup>232</sup>Th and <sup>238</sup>U are 158 Bq kg-1 and 80 Bq kg-1, respectively. These are more than 2.4 and 3.5 times, respectively higher than the world averages. Also notable are the high levels of <sup>40</sup>K in the mid-stream which were found to be as high as 979Bq kg-1 (see sample 9A in Table, Appendix X). This could be due to the presence of minerals rich in <sup>40</sup>K such as microcline and orthoclase which are found in igneous and metamorphic rocks (Kennedy, 2016). The activities of Th-232, U-238, and K-40 in the top and lower portions of all three bridges were compared by analysis; Kauwi (upstream), Tanganyika (midstream) and Tiva bridge (downstream) along the left and right banks and in the middle of the river. This is shown in Table 5.2 below. It was observed that the distribution of activities of each radionuclide, no particular trend observed.

*Table 5.2 Summary of average activity concentration along the river Tiva*

Location	Along the left bank			In the middle			Along the right bank		
	Th-232	U-238	K-40	Th-232	U-238	K-40	Th-232	U-238	K-40
Kauwi(upstream)	26	28	661	18	34	579	15	26	555
Tanganyika(midstream)	8	8	679	12	7	630	23	13	690
Tiva (downstream)	21	28	579	19	32	540	20	28	615

The activity concentrations of  $^{238}\text{U}$  and  $^{232}\text{Th}$  were calculated from gamma photo peaks of  $^{214}\text{Pb}$  (351KeV) and  $^{212}\text{Pb}$  (238 KeV) for uranium and thorium respectively while that of  $^{40}\text{K}$  was evaluated from the 1460KeV gamma line. Fig. 5.1 displays a classic HPGe gamma spectrum for sample AS1, obtained from downstream Tiva river.

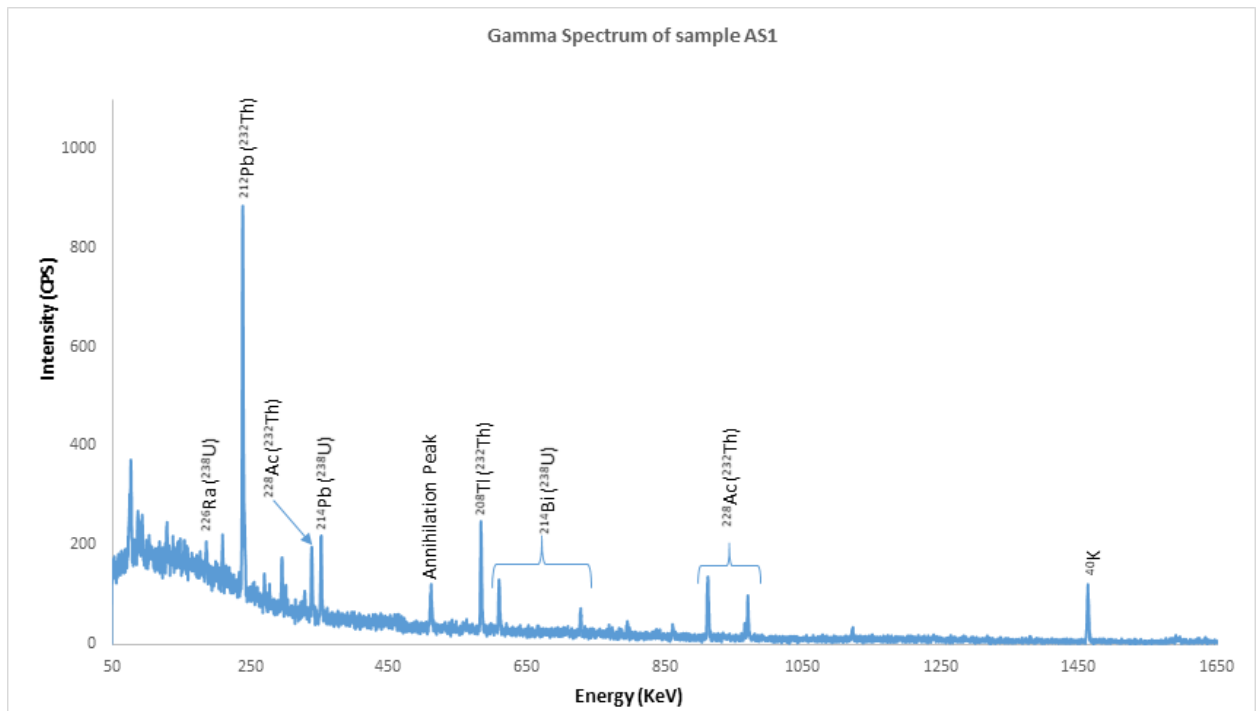


Figure 5.1 Typical gamma ray spectrum of sand sample from downstream of river Tiva

### 5.3. External Dose Rates Distributions along Tiva River

The maps below show the results of the distribution of dose rates in the upstream, midstream and downstream sections.

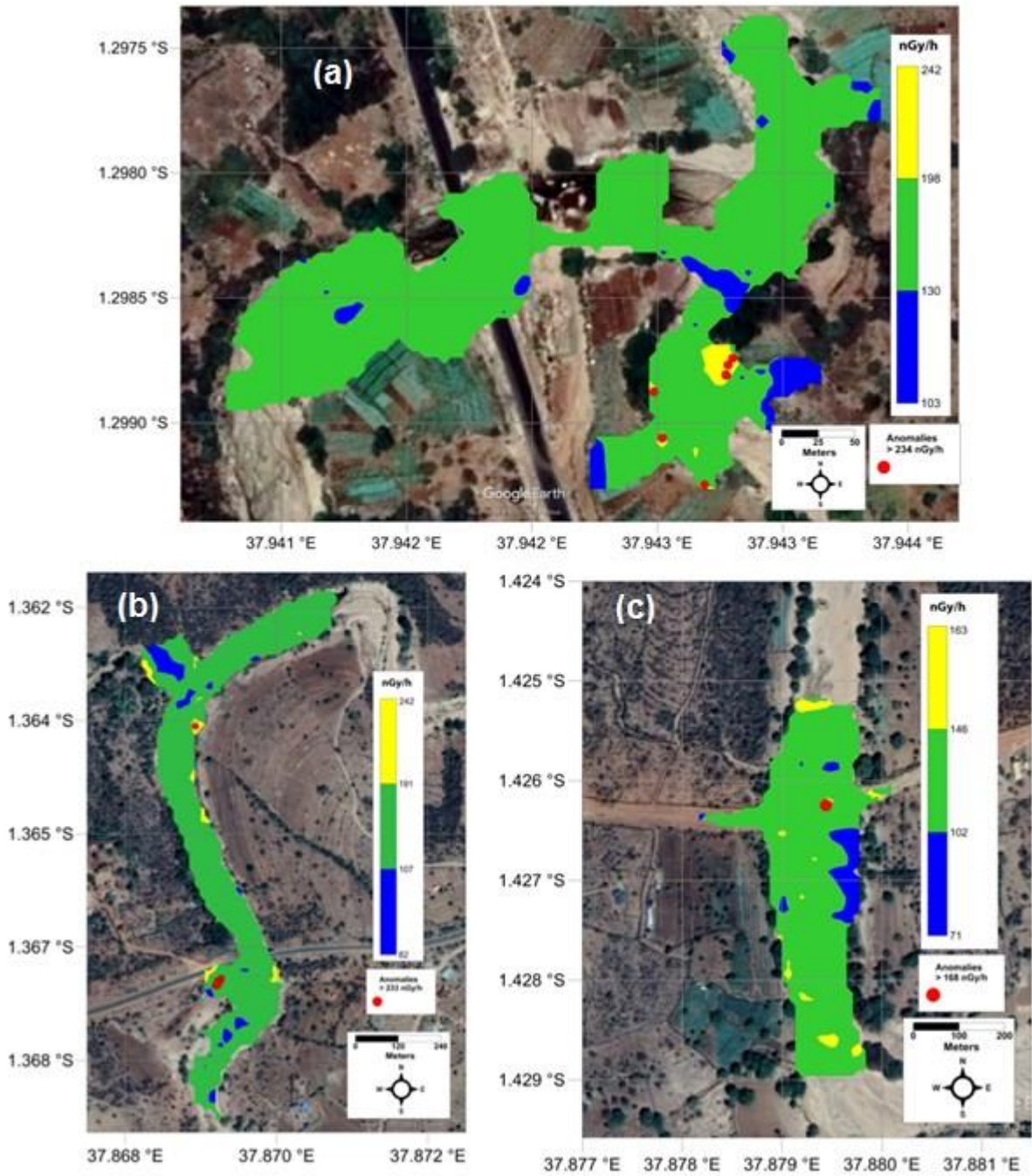


Figure 5.2 Dose distribution at (a) Kauwi bridge (upstream), (b) Tanganyika bridge (midstream) and (c) Tiva bridge (downstream)

Based on the histograms (refer to the appendix), the distribution of dose rates was found to be normal, indicating the absence of hotspots and suggesting that the radiation in the area is primarily from natural background sources (NORM). In the upstream region, most of the monitored areas had dose rates ranging from 130 to 198 nSv/h, with a few isolated areas

showing anomalies (refer to Fig. 5.2) where values exceeded the mean of 164 nSv/h (considered as the background radiation level for the site). This could be attributed to the collection of sands with higher activity concentrations of natural radionuclides, as indicated by the mineralogy study conducted by (Kennedy, 2016), which revealed the presence of sedimentary and igneous rocks. Additionally, there were a few areas with lower dose rates ranging from 103 to 130 nSv/h (refer to Fig. 5.2), potentially due to patches of water that provide shielding from radiation for the sands.

The same dose rate distribution pattern was found in both the midstream and downstream with lower mean dose rates of 149nSv/h and 124nSv/h, respectively; this shows that there is a decrease of radiation exposure downstream. This trend could be attributed to either natural factors or anthropogenic activities. For instance, the locals have dug water points on the base of the river for irrigating small scale farms adjacent to the river. Fig 5.3 shows dose-rate measurements extended to the environs, on a perimeter of about 5km along Tiva-Kitui-Machakos road adjacent to the Tiva River channel.

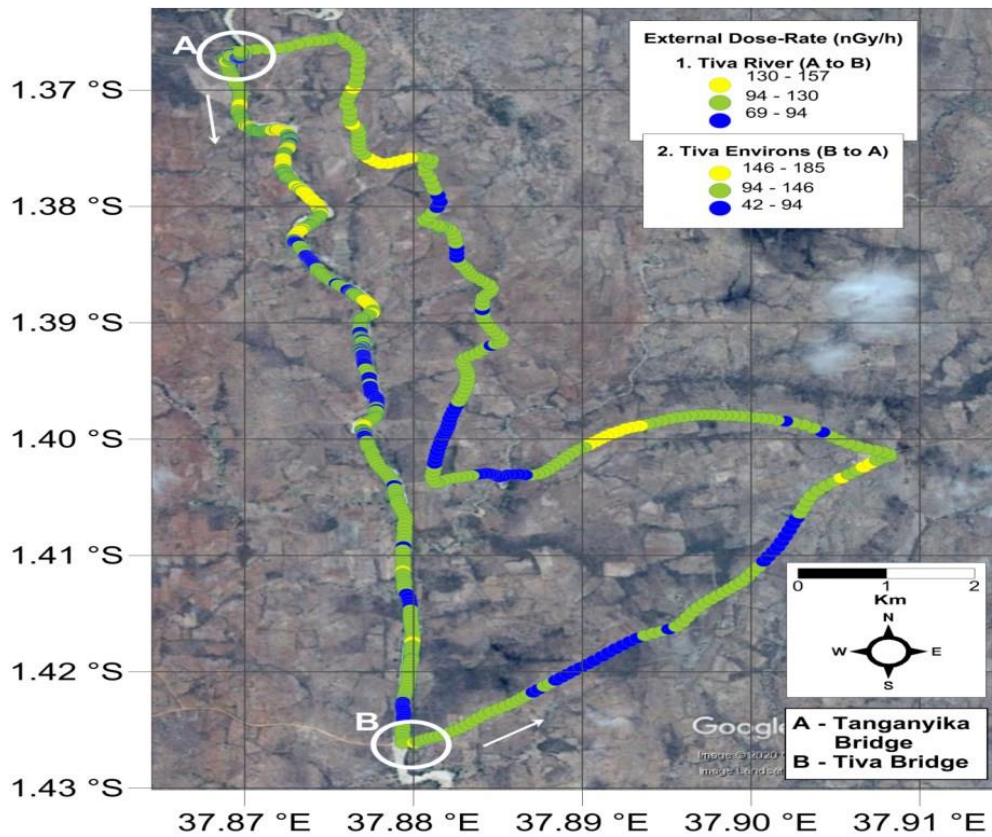


Figure 5.3 Dose rate of environs of Tiva River

The data revealed a relatively lower mean dose rate of 120 nSv/h, indicating a decrease in radiation exposure. Interestingly, the highest dose rates were observed at the midstream section, specifically at Tanganyika bridge. Local interviews conducted during the research indicated that sand harvesting activities take place in this area, which could explain the elevated dose rates. A summary of the maximum, minimum, and mean dose rates observed in all the study areas is presented in Table 5.3.

*Table 5.3 Summary of dose rate measurements along Tiva River*

<b>Section of the river</b>	<b>No. of measurements</b>	<b>Min. Dose rate, nSv/h</b>	<b>Max. Dose rate, nSv/h</b>	<b>Mean dose rate, nSv/h</b>
Upstream	836	97	289	164±36
Mid-stream	1751	46	342	149±42
Mid-downstream	512	69	157	112±18
Downstream	521	65	171	124±22
Environs	576	101	185	120±26

It can be seen that both the lowest and highest dose rates are found at the mid-stream section, 46 nSv/h and 342nSv/h respectively. However, the upstream has a relatively higher activity at 164±36 nSv/h compared to midstream 149±42 nSv/h and downstream at 124±22 nSv/h. Thus the dose rate increases from downstream to upstream. This may be attributed to the activities of K-40 in the three sections.

#### **5.4. Correlation between Dose Rate and Radioactivity Concentrations**

The maps below show selected demarcated sites.



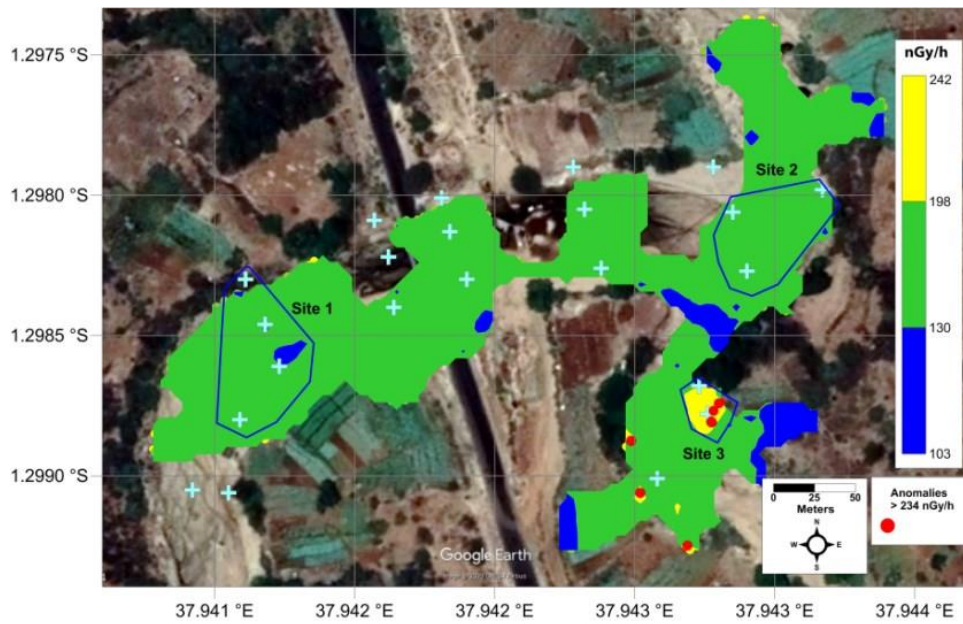


Figure 5.4 Demarcations upstream

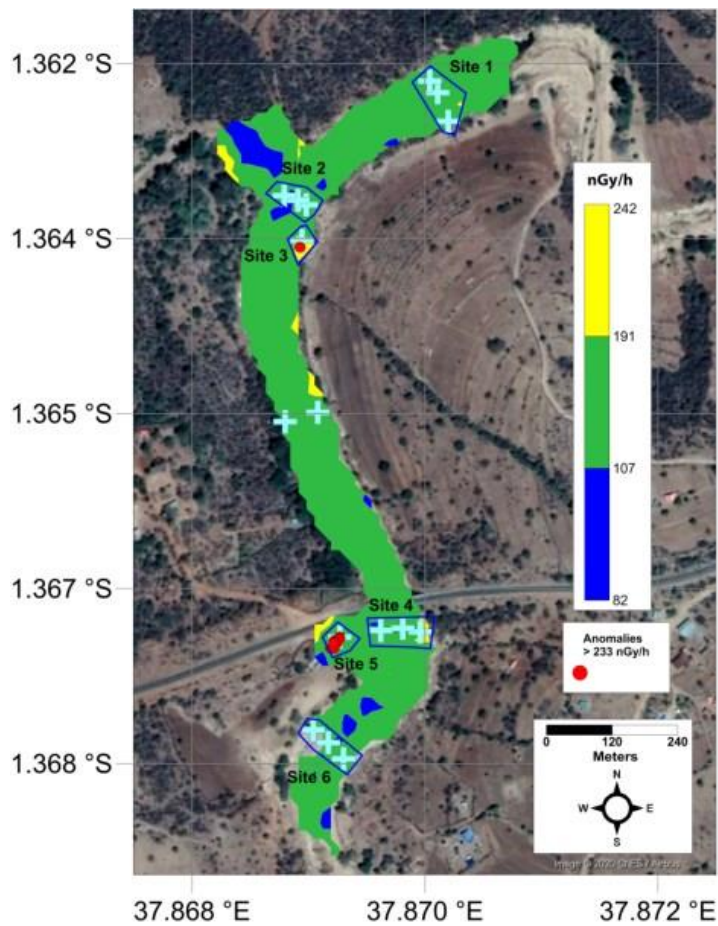


Figure 5.5 Demarcations upstream

Table 5.4 displays the activity concentrations of natural radionuclides and the accompanying dose rates.

*Table 5.4 Dose rates (nSv/h) and activity concentrations (BqKg-1) of demarcated sites*

	<b>Dose rate</b>	<b>Th-232</b>	<b>U-238</b>	<b>K-40</b>
TM_Site 01	152	23	11	420
TM_Site 04	154	11	11	584
TU_Site 01	226	18	34	560
TU_Site 02	211	19	25	610
TU_Site 03	272	26	15	898

It can be observed that the nuclide K-40 values are above world average of 400Bq kg-1 in all the demarcated sites. These high levels of activity concentration may be the major contribution to the corresponding dose rates since the concentrations of U-238 and Th-232 are lower than the global averages of 30 and 35 Bq kg -1 respectively. The highest activity concentration of K-40 is found at site 3 which corresponds to an isolated hot spot in the midstream. Fig 5.6 (a), (b) and (c) show the correlation between the radionuclides and the corresponding dose rates. There was a strong correlation of 0.7 between the dose rate and K-40 compared to correlation of 0.3 and 0.2 due to Th-232 and U-238 respectively. This indicates the presence of igneous, and metamorphic rocks which house minerals rich in potassium such as orthocase and microline (Kennedy, 2016).



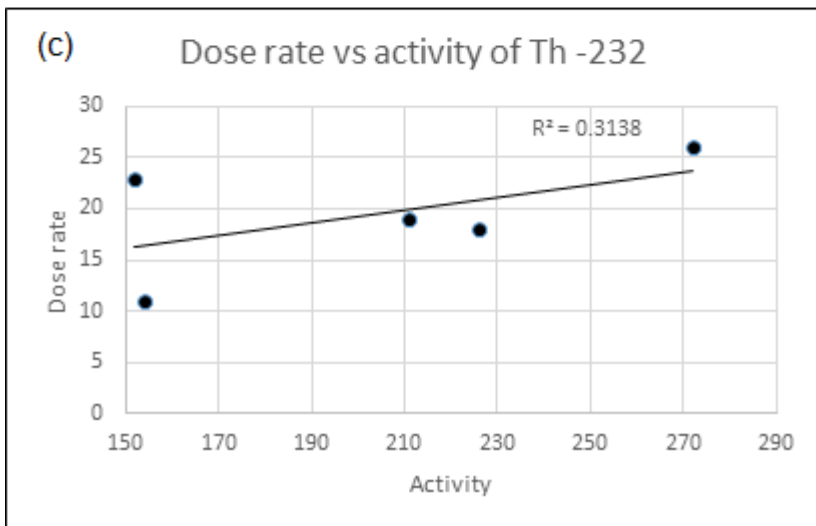
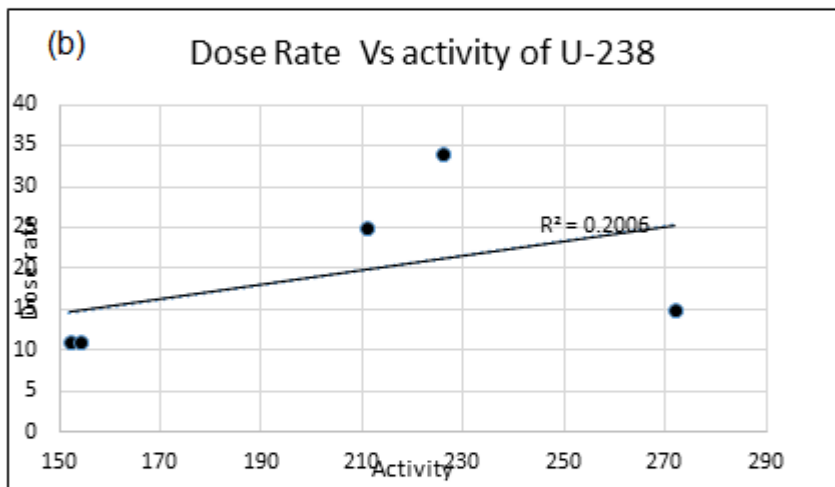
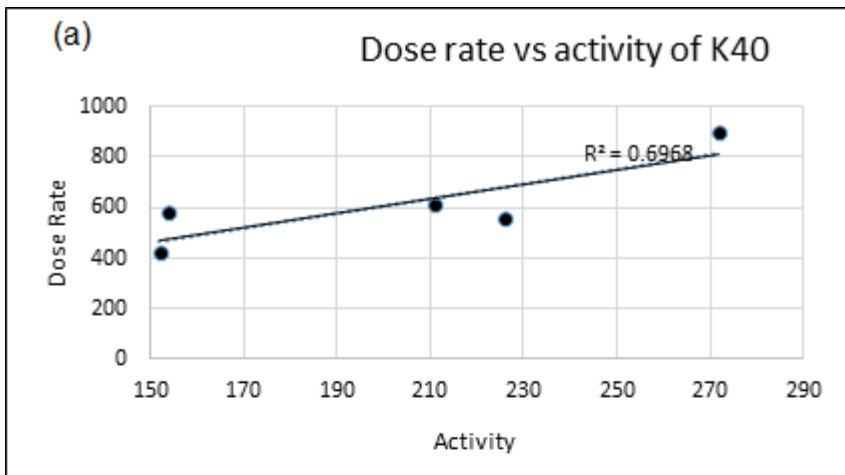


Figure 5.6 Correlation between radioactivity concentrations and absorbed gamma dose rates in the study area

## 5.5. Elemental Concentrations

### 5.5.1. Comparison of measured results with certified values

On certified reference materials, EDXRF measurements were made, and the outcomes were equated to the measured values in Table 5.5.

*Table 5.5 Detection limits and comparison of measured and certified values*

<b>Element</b>	<b>DL (ppm)</b>	<b>Certified (ppm)</b>	<b>SD of Cert (ppm)</b>	<b><math>U_{CRM}</math> (k=1.5)</b>	<b>Measured Median (ppm)</b>	<b>MAD</b>	<b><math>U_m</math></b>	<b><math>\Delta_m</math> (ppm)</b>	<b><math>U_\Delta</math> (ppm)</b>	<b>No Significant Difference between Meas &amp; Certified</b>
K	2600	19500	1060	707	14700	800	462	4800	7233	TRUE
Ca	1600	13800	790	527	12100	100	58	1700	2551	TRUE
Ti	700	4300	290	193	4113.6	5.2	3	186	280	TRUE
Mn	150	1000	80	53	1043.2	16.1	9	43	66	TRUE
Fe	90	29700	1510	1007	30000	300	173	300	520	TRUE
Ni	60	37.9	5.3	4	401.7	0.7	0	364	546	TRUE
Cu	30	20.1	3.1	2	329.7	8.9	5	310	464	TRUE
Zn	30	96.1	11.6	8	91.3	11	6	5	12	TRUE
Rb	10	107	12.7	8	123.5	0.3	0	17	25	TRUE
Sr	10	106	12.6	8	124.5	1.3	1	19	28	TRUE
Y	10	31.8	4.5	3	33.2	0.3	0	1	2	TRUE
Zr	10	302	30.7	20	323	0.6	0	21	32	TRUE
Pb	10	36.9	5.1	3	47.6	2.3	1	11	16	TRUE

It was determined that no major difference between the measured and certified values existed and this was denoted as TRUE for all the elements.

### 5.5.2. Elemental concentrations along the Tiva River

Tables 5.6 - 5.8 below shows the descriptive statistics of the elemental concentrations in the three sections of study namely; upstream midstream and downstream which includes mean concentration values minimum and maximum concentrations in each section, standard deviation, skewness and kurtosis each element. The results of elemental concentrations for the individual samples in the three sections of the river selected for study are shown in the Tables A2 – A4 (Appendix 5).

*Table 5.6 Descriptive statistics of the elements found in the upstream. (Concentrations are in ppm)*

<b>Element</b>	<b>No. of observations</b>	<b>Mean</b>	<b>Maximum</b>	<b>Minimum</b>	<b>Stdev</b>	<b>Skewness</b>	<b>Kurtosis</b>
<b>K</b>	40	19305.6	28100.0	13400.0	2474.9	0.8	1.0
<b>Ca</b>	40	7235.3	11100.0	4179.7	1331.8	0.5	1.4
<b>Ti</b>	40	4811.0	8317.3	2305.8	1263.1	0.7	-0.4
<b>Mn</b>	40	453.8	638.8	333.2	78.8	0.6	-0.5
<b>Fe</b>	40	28069.4	40600.0	17800.0	282.8	0.2	-0.7
<b>Ni</b>	40	337.8	376.8	309.5	6.9	0.4	-0.4
<b>Cu</b>	40	288.0	315.6	258.9	0.6	0.1	-0.6
<b>Zn</b>	40	35.8	39.8	30.6	0.0	-0.3	-1.9
<b>Rb</b>	40	46.0	56.4	32.1	2.3	-0.4	-0.5
<b>Sr</b>	40	686.4	809.7	504.0	2.3	-0.6	1.7
<b>Y</b>	40	10.7	11.9	10.1	0.0	1.7	3.0
<b>Zr</b>	40	196.9	409.2	88.7	54.7	1.2	2.4
<b>Pb</b>	40	17.5	23.1	13.4	0.4	0.5	-0.8

*Table 5.7 Descriptive statistics of elements found in the midstream (concentrations are in ppm)*

<b>Element</b>	<b>No. of observations</b>	<b>Mean</b>	<b>Maximum</b>	<b>Minimum</b>	<b>Stdev</b>	<b>Skewness</b>	<b>Kurtosis</b>
<b>K</b>	23	8874.4	15800.0	3058.2	2881.3	-0.1	-1.4
<b>Ca</b>	23	7613.9	11800.0	4607.3	470.4	0.7	-0.3
<b>Ti</b>	23	16581.7	46900.0	3596.3	12419.0	0.9	0.1
<b>Mn</b>	23	539.3	1225.2	255.9	101.8	1.2	1.1
<b>Fe</b>	23	39841.3	104900.0	12300.0	26021.5	0.9	0.0
<b>Ni</b>	23	256.1	333.7	182.7	10.5	0.1	0.5
<b>Cu</b>	23	241.0	307.2	195.0	21.2	0.2	-0.8
<b>Zn</b>	23	54.6	96.4	31.5	0.0	0.8	0.2
<b>Rb</b>	23	25.0	40.8	15.8	0.0	0.8	0.8
<b>Sr</b>	23	450.8	592.0	219.5	66.5	-0.6	-0.6
<b>Y</b>	23	19.9	29.5	11.3	0.0	0.3	Z 1.2
<b>Zr</b>	23	1507.1	4501.4	234.4	1568.2	1.2	1.0
<b>Pb</b>	23	17.6	23.1	10.9	2.2	-0.4	-0.4

*Table 5.8 Descriptive statistics of elements found in the downstream (concentrations are in ppm)*

<b>Element</b>	<b>No. of observations</b>	<b>Mean</b>	<b>Maximum</b>	<b>Minimum</b>	<b>Stdev</b>	<b>Skewness</b>	<b>Kurtosis</b>
<b>K</b>	18	19011.3	25100.0	12900.0	2333.5	0.1	-0.6
<b>Ca</b>	18	9516.6	28700.0	6127.8	565.7	3.4	12.8
<b>Ti</b>	18	17351.3	122600.0	3343.9	4737.6	3.9	15.7
<b>Mn</b>	18	753.9	2577.3	460.5	156.0	3.5	13.2
<b>Fe</b>	18	59570.0	247700.0	27500.0	17748.4	3.4	12.9
<b>Ni</b>	18	350.0	502.4	275.0	39.3	2.1	6.6
<b>Cu</b>	18	314.0	464.6	259.8	32.0	2.2	6.7
<b>Zn</b>	18	55.8	209.3	32.5	9.4	3.6	13.9
<b>Rb</b>	18	38.6	62.9	26.3	3.3	0.6	1.7
<b>Sr</b>	18	706.1	1163.5	532.1	43.2	1.3	4.4
<b>Y</b>	18	14.9	40.8	10.2	0.0	3.1	10.2
<b>Zr</b>	18	471.8	2513.6	147.6	95.5	3.8	15.8
<b>Pb</b>	18	18.7	29.1	11.9	3.5	0.8	-0.1

From the results, it can be observed that there are high means of Fe (28,069) and K (19,305) in the upstream, Fe (39,841) and Ti (16,581) in the midstream, and Fe (59,570), K (19011) and Ti (17,351) in the downstream. This indicates that Fe is the most abundant element in the three sections with its maximum of 247,700ppm found in the downstream section of the river followed by Ti, maximum 122,600 ppm, found downstream and K with its maximum of

28,100ppm in the upstream section, see the representative EDXRF spectra of samples obtained from the three sections of the river in Fig 5.7.

The skewness, which describes the level of asymmetry of a distribution around the mean, was found to be varied in the three sections implying that the distribution of the elements in each section is different. However, all the elements are positively skewed with the exception of Zn, Rb and Sr which further implies that most of the elements are correlated and exhibit same formation factors.

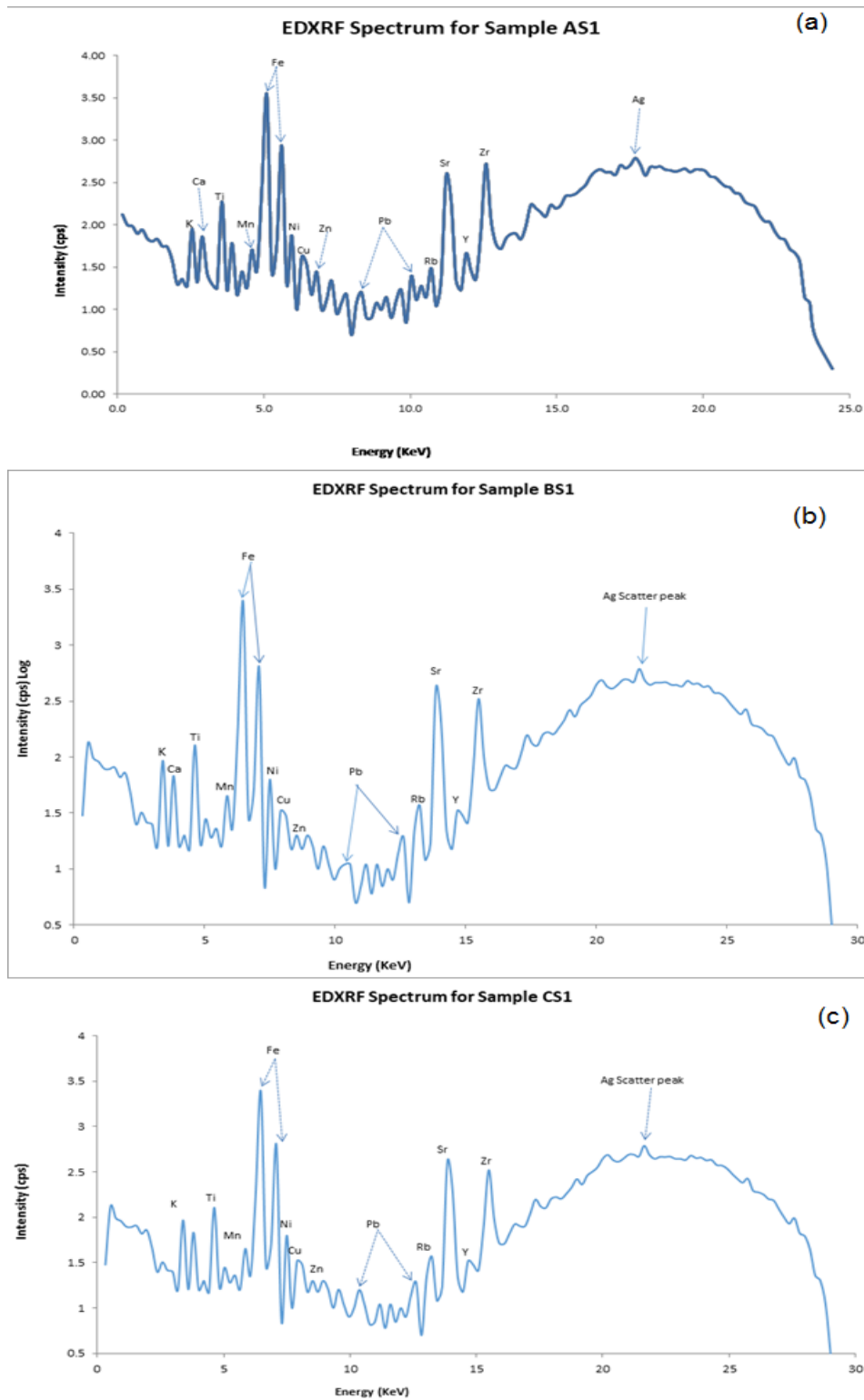


Figure 5.7 Spectrum for sand samples obtained from Tiva river at (a) upstream, (b) midstream and (c) downstream.

From the correlation matrix of the elemental concentrations (see Table 5.9), the elements may be seen to have positive coefficients in general and to be strongly associated, with the

strongest connections occurring for the couples, Fe-Mn, Fe-Ti, Zn-Ti, Fe-Zn and Ti-Fe. The aforementioned correlations imply a shared origin and/or chemical similarity. It was observed that Mn, Fe, Zn and Ti have a high correlation ( $> 0.9$ ) implying that they are found in the same parent rock. The negative correlations observed between Zr and K (-0.6), Zr and Sr (-0.7), and Zr and Rb (-0.7) indicated the pairs originated from different sources and therefore there is no association in their geochemical dynamics (Chandrasekaran *et al.*, 2015).



*Table 5.9 EDXRF Pearson correlation analysis results*

	<b>K</b>	<b>Ca</b>	<b>Ti</b>	<b>Mn</b>	<b>Fe</b>	<b>Ni</b>	<b>Cu</b>	<b>Zn</b>	<b>Rb</b>	<b>Sr</b>	<b>Y</b>	<b>Zr</b>
<b>K</b>	1	0.38	-0.01	0.20	0.13	0.71	0.61	0.07	0.82	0.82	-0.17	-0.57
<b>Ca</b>	0.38	1	0.81	0.82	0.79	0.61	0.66	0.81	-0.05	0.2	0.57	0.17
<b>Ti</b>	-0.01	0.81	1	0.95	0.96	0.49	0.6	0.98	-0.41	-0.24	0.87	0.61
<b>Mn</b>	0.2	0.82	0.95	1	0.99	0.67	0.76	0.96	-0.22	-0.07	0.8	0.45
<b>Fe</b>	0.13	0.79	0.96	0.99	1	0.64	0.74	0.97	-0.28	-0.13	0.83	0.5
<b>Ni</b>	0.71	0.61	0.49	0.67	0.64	1	0.95	0.56	0.42	0.48	0.35	-0.11
<b>Cu</b>	0.61	0.66	0.6	0.76	0.74	0.95	1	0.67	0.27	0.37	0.47	0.03
<b>Zn</b>	0.07	0.81	0.98	0.96	0.97	0.56	0.67	1	-0.34	-0.18	0.84	0.55
<b>Rb</b>	0.82	-0.05	-0.41	-0.22	-0.28	0.42	0.27	-0.34	1	0.84	-0.44	-0.72
<b>Sr</b>	0.82	0.2	-0.24	-0.07	-0.13	0.48	0.37	-0.18	0.84	1	-0.3	-0.65
<b>Y</b>	-0.17	0.57	0.87	0.8	0.83	0.35	0.47	0.84	-0.44	-0.3	1	0.79
<b>Zr</b>	-0.57	0.17	0.61	0.45	0.5	-0.11	0.03	0.55	-0.72	-0.65	0.79	1
<b>Pb</b>	0.03	0.27	0.31	0.29	0.27	0.17	0.18	0.31	0.02	0.02	0.31	0.17

### 5.5.3. Principal component analysis of EDXRF measurements along Tiva River

A principal component analysis was done on EDXRF measurements along Tiver river. Table 5.10 illustrates the percentage of variances preserved by each principal component, labelled as Dim 1-13, which correspond to the measured elements.

*Table 5.10 Eigen values and variances for principal components measured along Tiva River*

	<b>Eigenvalue</b>	<b>Variance.percent</b>	<b>Cumulative.variance.percent</b>
Dim.1	6.76	51.97	51.97
Dim.2	4.02	30.89	82.86
Dim.3	0.93	7.15	90.01
Dim.4	0.48	3.71	93.72
Dim.5	0.35	2.70	96.43
Dim.6	0.15	1.19	97.61
Dim.7	0.10	0.80	98.42
Dim.8	0.07	0.51	98.92
Dim.9	0.05	0.40	99.32
Dim.10	0.04	0.30	99.62
Dim.11	0.03	0.23	99.86
Dim.12	0.01	0.09	99.94
Dim.13	0.01	0.06	100.00

It was observed that the first two PCs, Dim 1 and 2, accounted for the highest variance in the measurements. 84% of total variability was accounted for by two principal components (PCs) and two trends in the data (see Fig. 5.8 (a)). The degree of correlation between each variable and each factor is indicated by the loading on each factor (See Fig. 5.8 (b)). PC1 accounted for 53% of the variance among the elements. The presence of Fe, Mn, Zn, and Ti in this group suggests that they are distinguished by their natural geochemical associations in the river basin. PC2 represented the abundance of Rb, Sr, K, and Zr concentrations in the samples explaining 31% of the variation and distinguishing samples from different river sections (upstream, midstream and downstream). The strong association of Fe and Mn in PC1

with Zn, Ti, Y, Ca, and Cu suggests that these elements were formed in the drainage basin by rock weathering. These associations could also be attributed to the role of Fe-Mn oxides as heavy metal carriers (Singh *et al.*, 1984).

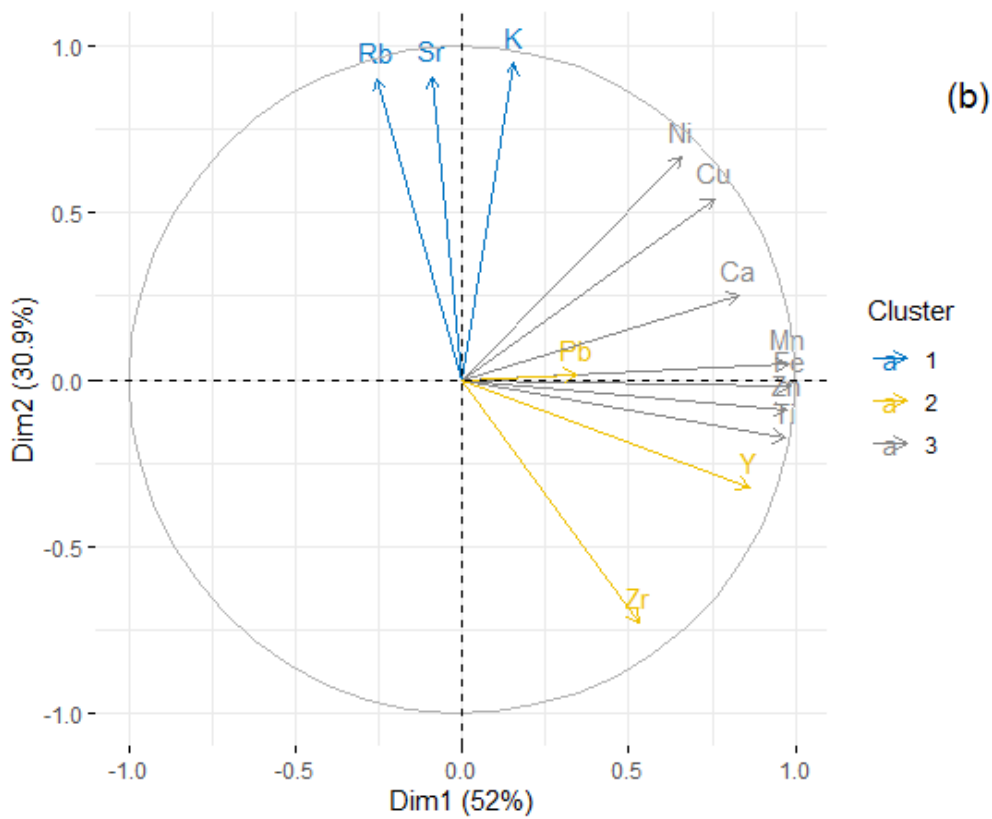
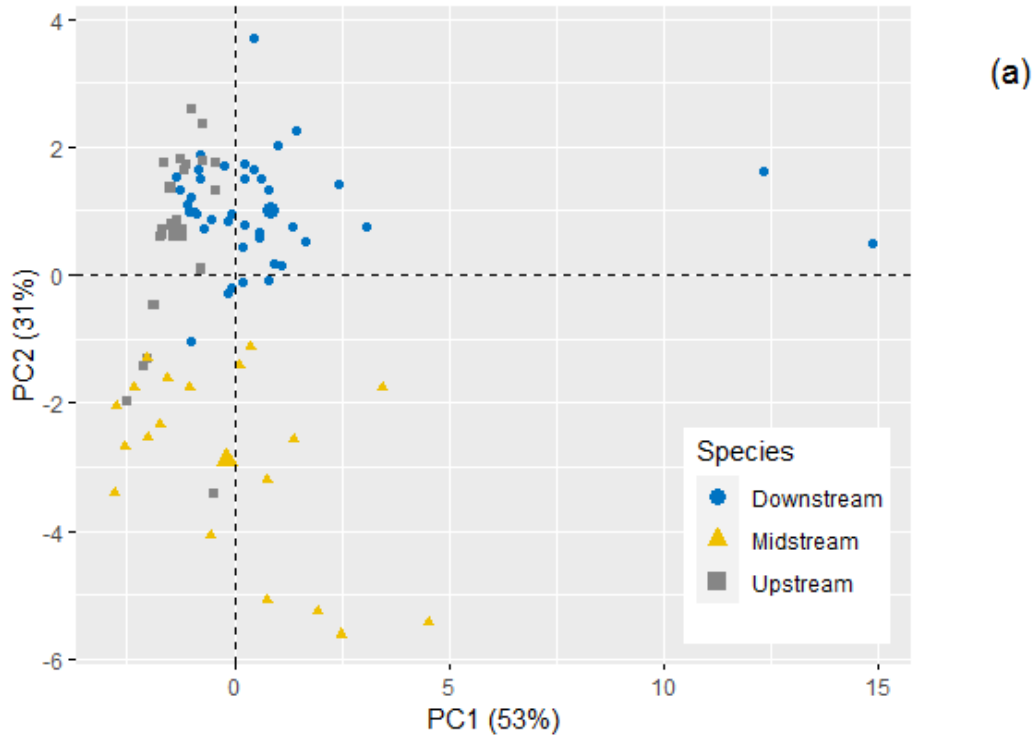


*Figure 5.8 PCA results of Tiva river elemental data (a) Scores plot and (b) Loadings plot*

From the score plot in Fig 5.8(a) it can be observed that PC1 is totally dominated by midstream and downstream samples. As shown by the loadings plot (Fig 5.8(b)) Mn, Fe, Zn, and Ti have higher concentrations compared to the upstream. All the midstream samples are in the negative of part of the PC2 and from the loadings plot Rb, Sr and K are the principal components in PC2 and are in high concentrations in PC2 and therefore have low concentrations. There are three clusters that can be observed namely; (Rb, Sr, K) in the downstream. This demonstrates a pattern in the river's course that aids in identifying the variables influencing the dispersion pattern of heavy metals throughout the river.

#### **5.5.4. Spatial distribution of heavy metal in Tiva sands**

Fig. 5.9 shows the results of spatial variation in the elements (identified as having the highest variation in the PCs; PC1 (53%) and PC2 (31%)), as well as NORM ( $^{40}\text{K}$ ,  $^{232}\text{Th}$  and  $^{238}\text{U}$ ) in the three sections of the river. Most PC1 elements and radionuclides have high values in the river's downstream region. The significant contribution of the river waters draining the mineralized areas upstream is reflected in these high values. The meanders visible between the river's upstream and mid-stream sections (see Fig. 5.10) may be responsible for the decrease in PC2 element concentrations, as well as U-238 and Th-232 (see Fig.5.10), caused by erosion and depositional activity on the river's outer and inner edges (Hooke, 2008).

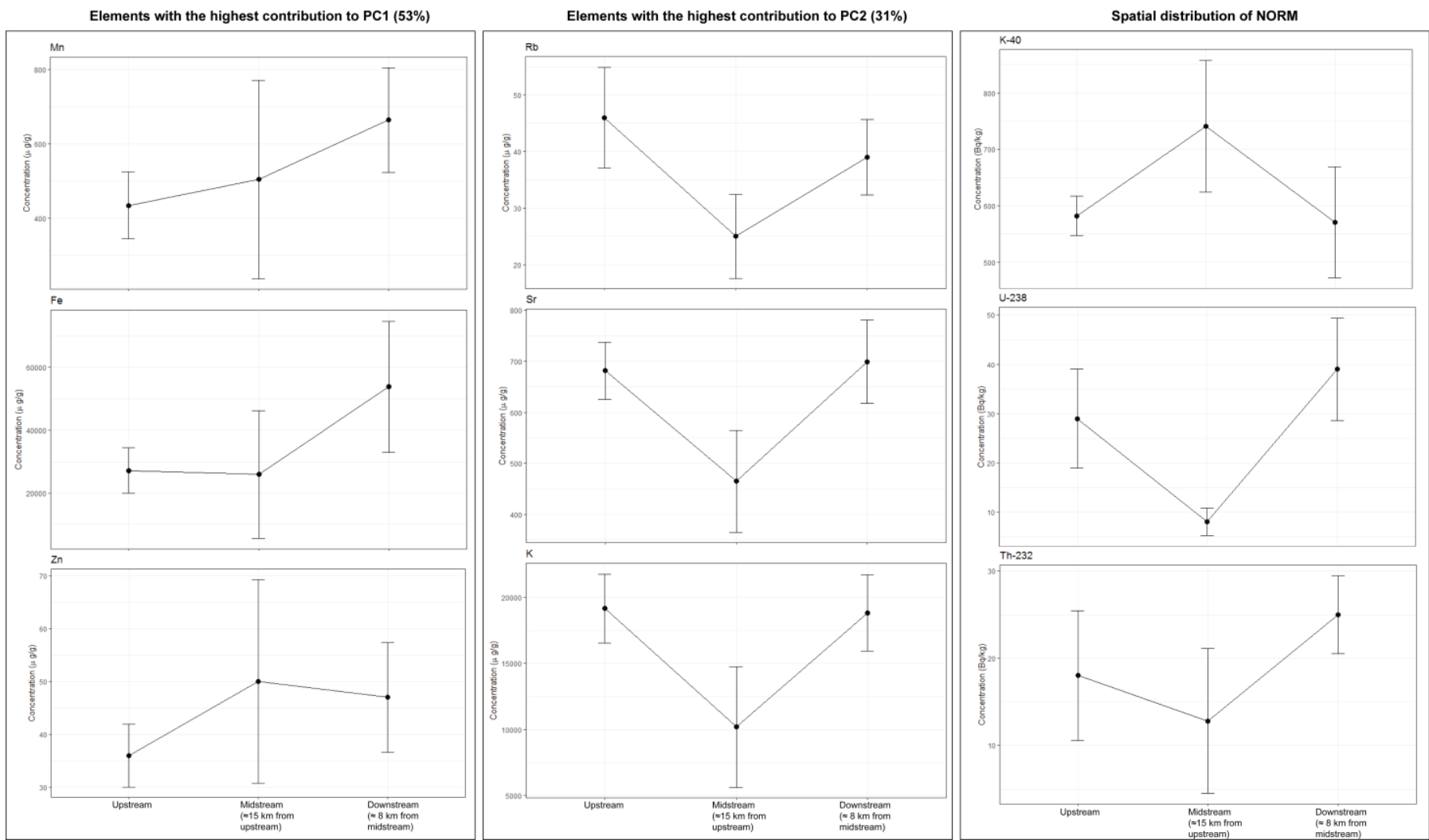


Figure 5.9 Downstream variation in the heavy metal and radionuclide concentrations in Tiva river

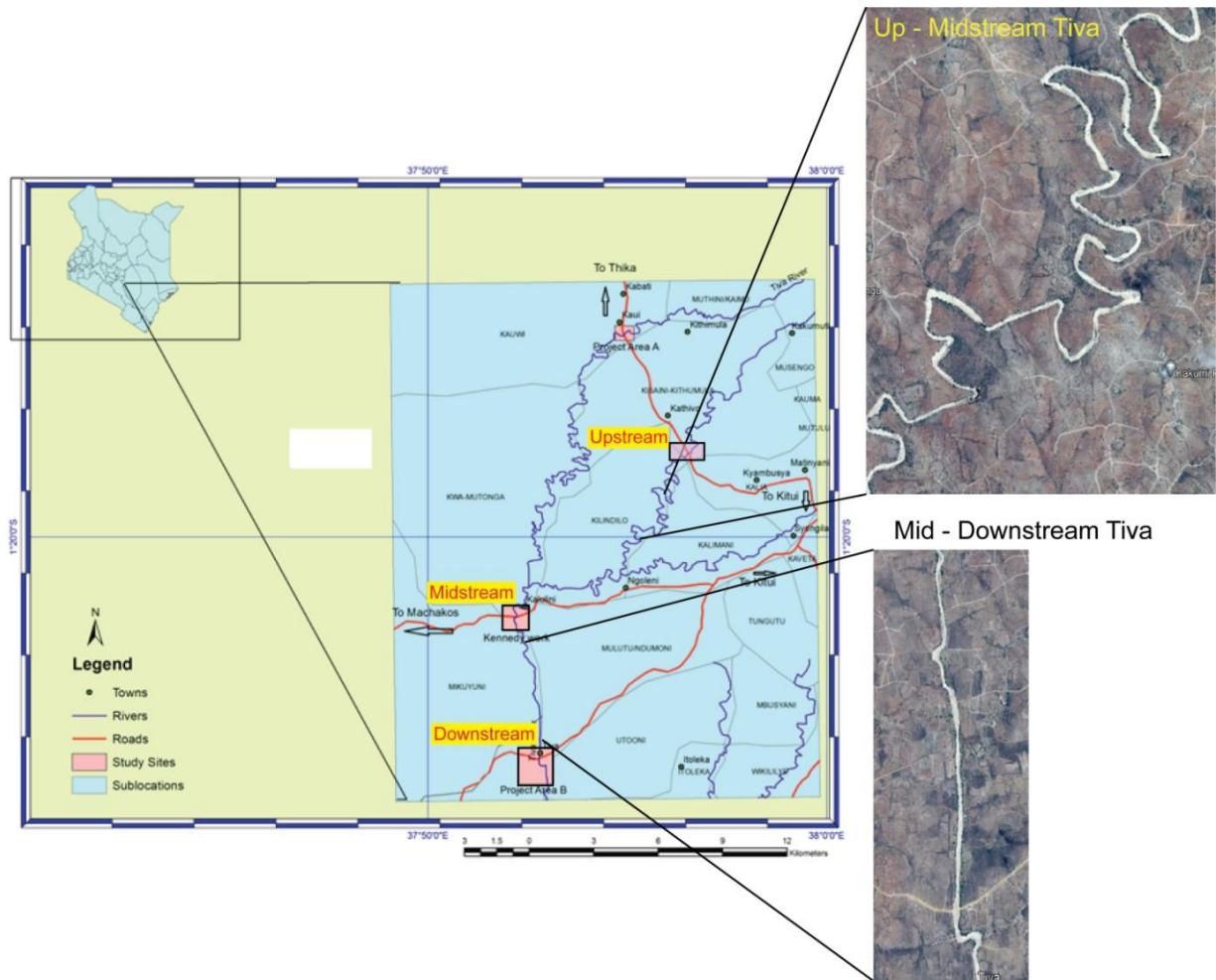


Figure 5.10 Map of the study area illustrating the terrain between the upstream and downstream sections of Tiva river

## CHAPTER 6: CONCLUSIONS AND RECOMMENDATIONS

### 6.1. Conclusions

In conclusion, the study has determined that sediment samples collected from the three selected sites along the Tiva River contain the primordial radionuclides  $^{40}\text{K}$ ,  $^{232}\text{Th}$ , and  $^{238}\text{U}$ . In comparison to global average values, the study reveals lower levels of  $^{238}\text{U}$  and  $^{232}\text{Th}$ , while  $^{40}\text{K}$  levels are up to 1.6 times higher. Consequently, utilizing sand from the Tiva water channel as a construction material is deemed safe and does not pose significant radioactive health risks. The average external gamma dose rates at the three sites, measured 1 meter above the ground, are as follows:  $164\pm 36$  nGy/h,  $149\pm 42$  nGy/h, and  $124\pm 22$  nGy/h, respectively. This represents an average of 2.5 times higher than the global average of 59 nGy/h, which increases the risk of radiation exposure for the local population.

Furthermore, it was determined that the primary heavy mineral present in the Tiva Sands is iron (Fe), followed by potassium (K), titanium (Ti), calcium (Ca), zirconium (Zr), manganese (Mn), copper (Cu), strontium (Sr), zinc (Zn), yttrium (Y), and lead (Pb). The high concentrations of Fe (39841ppm), K (19305ppm), Ti (17351ppm), Ca (9516ppm), and Zr (1507ppm) indicate the presence of minerals such as hematite, albite, quartz, orthoclase, ilmenite, and microcline in the sands. In comparison to the results obtained by (Kennedy, 2016) in the midstream section, the concentrations of Fe (73,135ppm), Ti (22,976ppm), and Zr (1115ppm) were higher. This difference is likely due to the influence of river flow during rainy seasons. The primary source of these minerals is the granitic rocks that predominantly exist in the drainage basin (Kennedy, 2016). The transportation of heavy metals (HM) and naturally occurring radioactive materials (NORM) in the Tiva River is significantly influenced by seasonal flooding during the rainy

seasons, the terrain of the river channel, and the geochemistry of elements in the riverine environment. Moreover, the concentrations of HM vary significantly, possibly as a result of variances in sediment composition, the non-uniform grain size distribution of the sands, and natural as well as anthropogenic factors that contribute to sorption (Vaithiyanathan *et al.*, 1992).

## **6.2. Recommendations and Future Work**

A similar study is recommended for a wider coverage on the environs of Tiva river. This should be extended to include radioactivity activities of soils and water sources such as boreholes. A further study on the objectives of this study should also be done further downstream and to find if water flow may have transported the heavy metals during heavy rains. A further study is also recommended to assess the situation further upstream and compare results with the upstream of this current study. This should include spatial distribution of elements so found. Further research, including chemical analyses of suspended and core sediments, as well as assessments of grain size fractions in surface sediments, is recommended to determine the vertical distribution and load of HM and NORM in Tiva river sediment profiles for pollution assessment.



## REFERENCES

- Achola, S.O., Patel, J.P., Mustapha, A.O. and Angeyo, H.K. (2012), Natural radioactivity and external dose in the high background radiation area of Lambwe east, southwestern Kenya, *Radiat. Prot. Dosimetry*, **Vol. 152 No. 4**, pp. 423–428.
- Adebiyi, F.M. and Ore, O.T. (2021), EDXRF analysis and risks assessment of potentially toxic elements in sand fraction (tailing) of Nigerian oil sands, *Energy, Ecol. Environ.*, Joint Center on Global Change and Earth System Science of the University of Maryland and Beijing Normal University, **Vol. 6 No. 3**, pp. 258–270.
- ATSDR. (1999), Agency for Toxic Substances and Disease Registry-ATSDR.
- Bouchard, M., Anzelmo, J., Rivard, S., Seyfarth, A., Arias, L., Behrens, K. and Durali-Müller, S. (2011), Global cement and raw materials fusion/XRF analytical solution. II, *Powder Diffr.*, **Vol. 26 No. 2**, pp. 176–185.
- Büchele, D., Chao, M., Ostermann, M., Leenen, M. and Bald, I. (2019), Multivariate chemometrics as a key tool for prediction of K and Fe in a diverse German agricultural soil-set using EDXRF, *Sci. Rep.*, **Vol. 9 No. 1**, pp. 1–11.
- Cen, P., Bian, X., Liu, Z., Gu, M., Wu, W. and Li, B. (2021), Extraction of rare earths from bastnaesite concentrates: A critical review and perspective for the future, *Miner. Eng.*, Pergamon, **Vol. 171**, p. 107081.
- Chandrasekaran, A., Ravisankar, R., Harikrishnan, N., Satapathy, K.K., Prasad, M.V.R. and Kanagasabapathy, K. V. (2015), Multivariate statistical analysis of heavy metal concentration in soils of Yelagiri Hills, Tamilnadu, India - Spectroscopical approach,

- Spectrochim. Acta - Part A Mol. Biomol. Spectrosc.*, Elsevier B.V., **Vol. 137**, pp. 589–600.
- Coggan, J.A., Melville, P.A., De Oliveira, C.M., Faustino, M., Moreno, A.M. and Benites, N.R. (2008), Microbiological and histopathological aspects of canine pyometra, *Brazilian J. Microbiol.*, **Vol. 39 No. 3**, pp. 477–483.
- Dwivedi, S.B., Kumar, R.R. and Srivastava, M. (2019), Multistage gedrite in gedrite–hypersthene-bearing high-grade granulites from Daltonganj, Chhotanagpur granite–gneissic complex, Jharkhand, as evident from TEM and textural relations, *J. Earth Syst. Sci.*, Springer India, **Vol. 128 No. 2**, pp. 1–14.
- Farai, I.P., Obed, R.I. and Jibiri, N.N. (2006), Soil radioactivity and incidence of cancer in Nigeria, *J. Environ. Radioact.*, **Vol. 90 No. 1**, pp. 29–36.
- Force, E.R. (1991), Geology of Titanium-Mineral Deposits, *Geol. Soc. Am.*, **No. 1**, available at: [specialpapers.gsapubs.org](http://specialpapers.gsapubs.org).
- Gauna, M.R., Rendtorff, N.M., Conconi, M.S., Suárez, G., Pasquevich, A., Rivas, P.C. and Damonte, L. (2017), Fine zircon (ZrSiO<sub>4</sub>) powder mechanical activation, a Perturbed Angular Correlation (PAC) analysis, *Prostaglandins, Leukot. Essent. Fat. Acids*, **Vol. 115**, pp. 60–66.
- Ghorbani, Y., Fitzpatrick, R., Kinchington, M., Rollinson, G. and Hegarty, P. (2017), A process mineralogy approach to gravity concentration of tantalum bearing minerals, *Minerals*, **Vol. 7 No. 10**, available at: <https://doi.org/10.3390/min7100194>.
- Gilmore, G.R. (2008), *Practical Gamma-Ray Spectrometry*, 2nd ed., John Wiley & Sons, Ltd,

England, available at:

<https://books.google.com/books?hl=en&lr=&id=S0Dy4hjkmmMC&oi=fnd&pg=PT12&ots=CGJtNmtIb8&sig=raumtguu1O5VVCthSCGEIHi3nNY>.

- Githenya, L.K. (2020), Geology and Economic Mineralization of the Neoproterozoic Mozambique Belt Rocks of the Mwitika-Makongo Area, Kitui County, South Eastern Kenya, **No. December 2020**, available at:<https://doi.org/10.13140/RG.2.2.33920.76808>.
- Gosen, B.S. Van, Fey, D.L., Shah, A.K., Verplanck, P.L. and Hoefen, T.M. (2014), Deposit Model for Heavy-Mineral Sands in Coastal Environments, *Miner. Depos. Model. Resour. Assessments U.S. Geol. Surv. Sci. Investig. Rep. 2010–5070–L*, p. 51 p.
- Grudzien, A., Kowalski, M. and Palka, N. (2018), Face re-identification in thermal infrared spectrum based on ThermalFaceNet neural network, *MIKON 2018 - 22nd Int. Microw. Radar Conf.*, Warsaw University of Technology, pp. 179–180.
- Grzebisz, W., Cieśla, L. and Diatta, J.B. (2001), Spatial Distribution of Copper in Arable Soils and in Non-Consumable Crops (Flax, Oil-Seed Rape) Cultivated Near a Copper Smelter, *Polish J. Environ. Stud.*, **Vol. 10 No. 4**, pp. 269–273.
- Harmsen, K. and Haan, F.A.M. de. (1980), Occurance and behaviour of uranium and thorium in soil and water, *Netherlands J. Agric. Sci.*, **Vol. 28 No. 1**, pp. 40–62.
- Hooke, J.M. (2008), Temporal variations in fluvial processes on an active meandering river over a 20-year period, *Geomorphology*, **Vol. 100 No. 1–2**, pp. 3–13.
- Hresc, J., Riley, E. and Harris, P. (2018), Mining project’s economic impact on local

- communities, as a social determinant of health: A documentary analysis of environmental impact statements, *Environ. Impact Assess. Rev.*, Elsevier, **Vol. 72 No. January**, pp. 64–70.
- IAEA. (2005), *Annual Report 2005*, Vienna, Austria, available at: <https://www.iaea.org/Worldatom/Documents/Anrep/Anrep2005>.
- Isinkaye, M.O. and Emelue, H.U. (2015), Natural radioactivity measurements and evaluation of radiological hazards in sediment of Oguta Lake, South East Nigeria, *J. Radiat. Res. Appl. Sci.*, Elsevier Ltd, **Vol. 8 No. 3**, pp. 459–469.
- Jibiri, N.N. and Okeyode, I.C. (2012), Evaluation of radiological hazards in the sediments of Ogun river, South-Western Nigeria, *Radiat. Phys. Chem.*, Elsevier, **Vol. 81 No. 2**, pp. 103–112.
- Jørgensen, N., Laursen, J., Viksna, A., Pind, N. and Holm, P.E. (2005), Multi-elemental EDXRF mapping of polluted soil from former horticultural land, *Environ. Int.*, **Vol. 31 No. 1**, pp. 43–52.
- Kang, X., Csetenyi, L. and Gadd, G.M. (2020), Monazite transformation into Ce- and La-containing oxalates by *Aspergillus niger*, *Environ. Microbiol.*, **Vol. 22 No. 4**, pp. 1635–1648.
- Kennedy, K.K. (2016), Characterization Of Sands For Heavy Minerals, Selected Heavy Metals Distribution And Profiling Along River Tiva, Kitui County, Southeastern Kenya, pp. 1–85.
- Kitheka, J.U., Obiero, M. and Nthenge, P. (2005), River discharge, sediment transport and exchange in the Tana Estuary, Kenya, *Estuar. Coast. Shelf Sci.*, **Vol. 63 No. 3**, pp. 455–468.

- Knoll, G.F. (1997), *Fast Neutron Cross Section Measurements*, Michigan.
- Krylov, D.P., Kuznetsov, A.B. and Gavrilova, A.A. (2020), Isotope Fractionation and the Pressure Effect on  $^{18}\text{O}/^{16}\text{O}$  in Kyanite-Sillimanite-Andalusite Polymorphs ( $\text{Al}_2\text{SiO}_5$ ): Ab-Initio Modelling, *Dokl. Earth Sci.*, **Vol. 491 No. 2**, pp. 235–237.
- Luderer, G., Pehl, M., Arvesen, A., Gibon, T., Bodirsky, B.L., de Boer, H.S., Fricko, O., *et al.* (2019), Environmental co-benefits and adverse side-effects of alternative power sector decarbonization strategies, *Nat. Commun.*, Springer US, **Vol. 10 No. 1**, pp. 1–13.
- Midigo, B.O. (2015), Radiological hazard assessment and investigation of heavy minerals of economic importance in Mwitia Syano river bed sands in Kitui.
- Misra, K.C. (2000), *Understanding Mineral Deposits*, 1st ed., Springer-Science+Business Media, B.V., Knoxville, U.S.A., available at:<https://doi.org/10.1007/978-94-011-3925-0>.
- Mohanty, A.K., Sengupta, D., Das, S.K., Saha, S.K. and Van, K. V. (2004), Natural radioactivity and radiation exposure in the high background area at Chhatrapur beach placer deposit of Orissa, India, *J. Environ. Radioact.*, **Vol. 75 No. 1**, pp. 15–33.
- Nasdala, L., Akhmadaliev, S., Burakov, B.E., Chanmuang N, C. and Škoda, R. (2020), The absence of metamictisation in natural monazite, *Sci. Rep.*, Nature Publishing Group UK, **Vol. 10 No. 1**, available at:<https://doi.org/10.1038/s41598-020-71451-7>.
- Nobi, E.P., Dilipan, E., Thangaradjou, T., Sivakumar, K. and Kannan, L. (2010), Geochemical and geo-statistical assessment of heavy metal concentration in the sediments of different coastal ecosystems of Andaman Islands, India, *Estuar. Coast. Shelf Sci.*, Elsevier Ltd, **Vol.**

**87 No. 2**, pp. 253–264.

Nong, D., Nguyen, T.H., Wang, C. and Van Khuc, Q. (2020), The environmental and economic impact of the emissions trading scheme (ETS) in Vietnam, *Energy Policy*, Elsevier Ltd, **Vol. 140 No. March**, p. 111362.

Nyamai, C.M., Mathu, E.M., Wallbrecher, E. and Opiyo-Akech, N. (2003), A Reappraisal of the Geology, Structures and Tectonics of the Mozambique Belt in Kenya East of the Rift System, *African J. Sci. Technol.*, **Vol. 4 No. 4**, p. 720.

Nzuki, A.D.K. (2017), Assessment of Heavy Metals in Soils in Block C, Mui Basin Kenya: Precoal Mining, *2017*, p. 2.

O'Garra, T. (2017), Economic value of ecosystem services, minerals and oil in a melting Arctic: A preliminary assessment, *Ecosyst. Serv.*, **Vol. 24**, pp. 180–186.

Otari, M. and Dabiri, R. (2015), Geochemical and environmental assessment of heavy metals in soils and sediments of Forumad Chromite mine, NE of Iran, *J. Min. Environ.*, **Vol. 6**.

Rafique, M., Rahman, S.U., Basharat, M., Aziz, W., Ahmad, I., Lone, K.A., Ahmad, K., *et al.* (2014), Evaluation of excess life time cancer risk from gamma dose rates in Jhelum valley, *J. Radiat. Res. Appl. Sci.*, Elsevier Masson SAS, **Vol. 7 No. 1**, pp. 29–35.

Reid, J.A. and Hou, B. (2006), Source of heavy minerals in the Eucla Basin palaeobeach placer province, South Australia: age data from detrital zircons, *MESA J.*, **Vol. 42**, pp. 10–14.

Reyneke, L. and Van Der Westhuizen, W.G. (2001), Characterisation of a heavy mineral-bearing sample from India and the relevance of intrinsic mineralogical features to mineral

- beneficiation, *Miner. Eng.*, **Vol. 14 No. 12**, pp. 1589–1600.
- Sack, R.O. and Ghiorso, M.S. (2019), Chromite as a petrogenetic indicator, *Oxide Miner. Petrol. Magn. Significance*, pp. 323–354.
- Schoeman, J.J. (1948), *A Geological Reconnaissance of the Area West of Kitui Township (with Coloured Geological Map)*, Government Printer, South Africa.
- Scott, R.D., MacKenzie, A.B. and Alexander, W.R. (1992), The interpretation of  $^{238}\text{U}$ - $^{234}\text{U}$ - $^{230}\text{Th}$ - $^{226}\text{Ra}$  disequilibria produced by rock-water interactions, *J. Geochemical Explor.*, **Vol. 45 No. 1–3**, pp. 323–343.
- Shah, B.R., Retnakaran, R. and Booth, G.L. (2008), Increased risk of cardiovascular disease in young women following gestational diabetes mellitus, *Diabetes Care*, **Vol. 31 No. 8**, pp. 1668–1669.
- Singh, S.K., Subramanian, V. and Gibbs, R.J. (1984), Hydrous Fe and Mn oxides — scavengers of heavy metals in the aquatic environment, *Crit. Rev. Environ. Control*, **Vol. 14 No. 1**, pp. 33–90.
- Strüder, L., Fiorini, C., Gatti, E., Hartmann, R., Holl, P., Krause, N., Lechner, P., *et al.* (1998), High Resolution Non Dispersive X-Ray Spectroscopy with State of the Art Silicon Detectors, *Mod. Dev. Appl. Microbeam Anal.*, **Vol. 19**, pp. 11–19.
- Taskin, H., Karavus, M., Ay, P., Topuzoglu, A., Hidiroglu, S. and Karahan, G. (2009), Radionuclide concentrations in soil and lifetime cancer risk due to gamma radioactivity in Kirklareli, Turkey, *J. Environ. Radioact.*, Elsevier Ltd, **Vol. 100 No. 1**, pp. 49–53.

- Teng, Y., Tuo, X., Ni, S., Zhang, C. and Xu, Z. (2003), Environmental geochemistry of heavy metal contaminants in soil and stream sediment in Panzhihua mining and smelting area, Southwestern China, *Chinese J. Geochemistry*, **Vol. 22 No. 3**, pp. 253–262.
- UNSCEAR. (2000), *SOURCES AND EFFECTS OF IONIZING RADIATION*, *J. Radiol. Prot.*, Vol. 21, available at:<https://doi.org/10.1088/0952-4746/21/1/609>.
- Vaithiyanathan, P., Ramanathan, A. and Subramanian, V. (1992), Sediment transport in the Cauvery River basin: sediment characteristics and controlling factors, *J. Hydrol.*, Elsevier, **Vol. 139 No. 1–4**, pp. 197–210.
- Wang, K., Li, W., Li, S., Tian, Z., Koefoed, P. and Zheng, X.Y. (2021), Geochemistry and cosmochemistry of potassium stable isotopes, *Geochemistry*, Elsevier GmbH, **Vol. 81 No. 3**, p. 125786.
- Wrixon, A.D. (2008), New ICRP recommendations, *J. Radiol. Prot.*, **Vol. 28 No. 2**, pp. 161–168.
- Yasmin, S., Barua, B.S., Khandaker, M.U., Kamal, M., Abdur Rashid, M., Abdul Sani, S.F., Ahmed, H., *et al.* (2018), The presence of radioactive materials in soil, sand and sediment samples of Potenga sea beach area, Chittagong, Bangladesh: Geological characteristics and environmental implication, *Results Phys.*, The Authors, **Vol. 8**, pp. 1268–1274.
- Yu, X.Y., Barnett, J.M., Amidan, B.G., Recknagle, K.P., Flaherty, J.E., Antonio, E.J. and Glissmeyer, J.A. (2018), Evaluation of nitrous oxide as a substitute for sulfur hexafluoride to reduce global warming impacts of ANSI/HPS N13.1 gaseous uniformity testing, *Atmos. Environ.*, Elsevier, **Vol. 176 No. August 2017**, pp. 40–46.



Zhai, K., Xue, W., Wang, H., Wu, X. and Zhai, S. (2020), Raman spectra of sillimanite, andalusite, and kyanite at various temperatures, *Phys. Chem. Miner.*, Springer Berlin Heidelberg, **Vol. 47 No. 5**, pp. 1–11.

## APPENDICES

### Appendix 1: Field study report

#### Report on additional sample collection of my MSc study

**Date:** 27th July 2014

**Site of study:** Tiva river near kwa Vonza, Kitui County

**Time left Nairobi:** 6.30am

**Time arrived on site:** 10.00am

**Personnel involved:** George Gitau

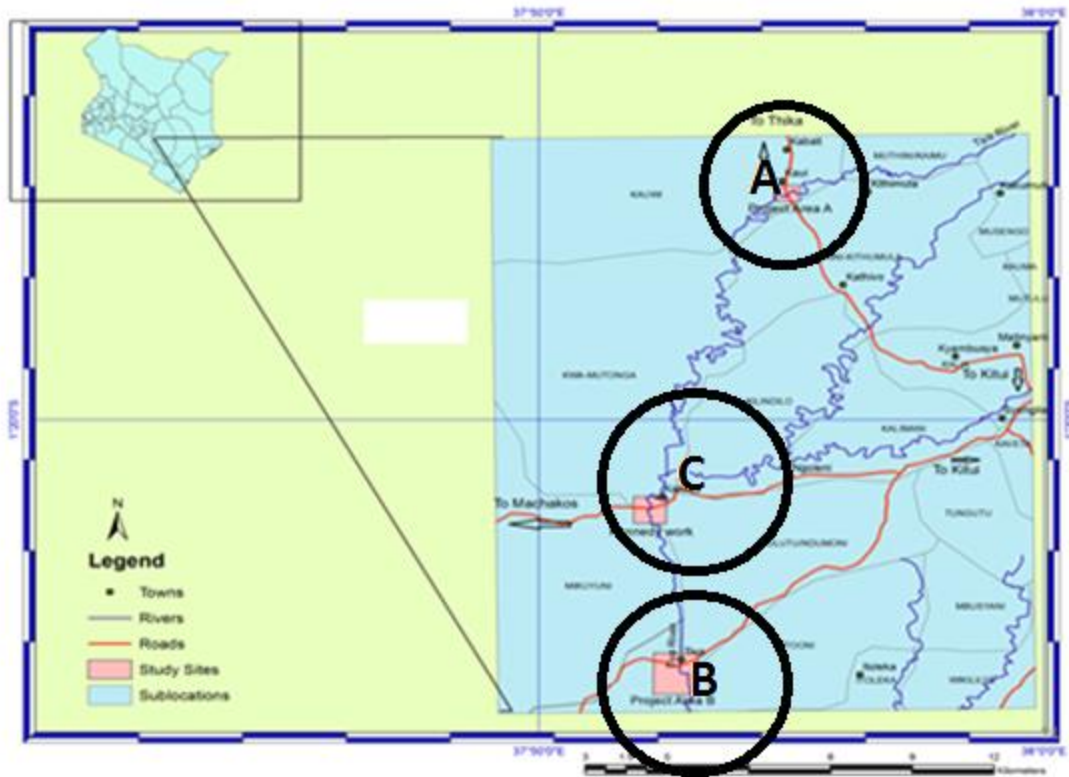
Dr Ian Kaniu (Supervisor)

Pamela Kageuza

Anthony Nzuki

**Purpose of visit:** To collect data on radiological concentrations along Tiva River using bGeiger Nano Kit. This was not done in the earlier data collection done in the river. Only sand samples were taken from area A and B and not from area C as shown below.

# Study area

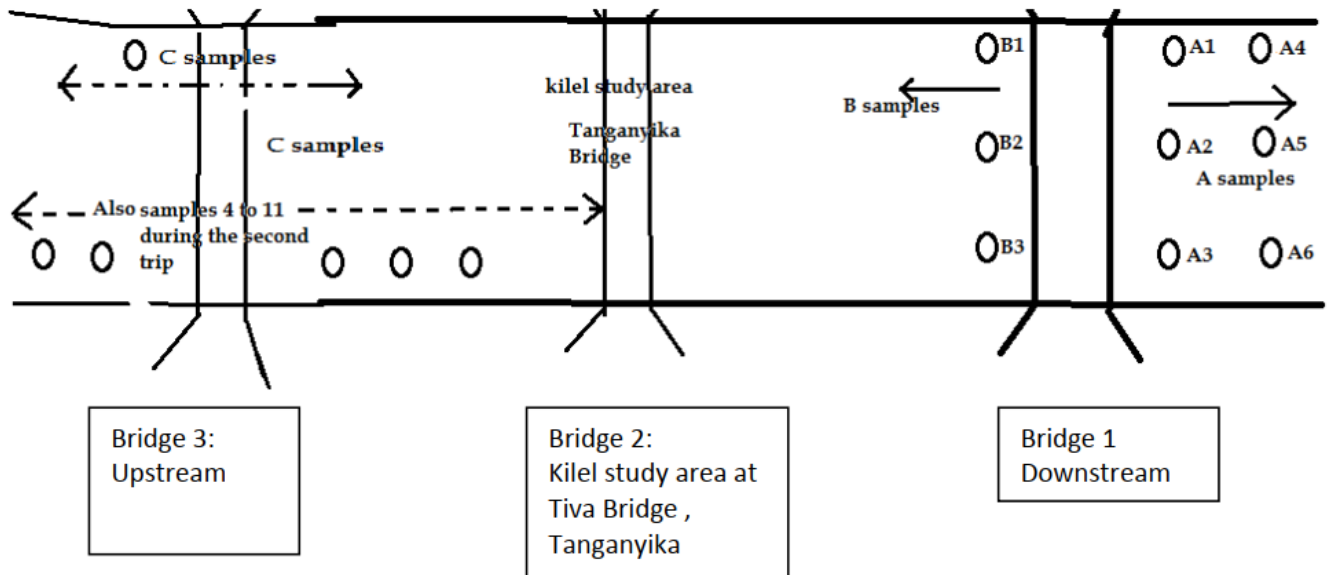


**GPS coordinates during the second visit**

Sample	Label	GPS Coordinates	Remarks	
1	4A	S01 . 32495 <sup>0</sup>	Hot spot	
		E037 .87020 <sup>0</sup>		
	4B	S01 . 36225 <sup>0</sup>	neighbor to hot spot 4A	
		E037 .87011 <sup>0</sup>		
	4C	S01 . 36215 <sup>0</sup>		
		E037 .87004 <sup>0</sup>		
2	5A	S01 . 36321 <sup>0</sup>		At the tributary of muwongo and tiva river mainstream
		E037 .86898 <sup>0</sup>		
	5B	S01 . 36317 <sup>0</sup>		
		E037 .86891 <sup>0</sup>		
	5C	S01 . 36313 <sup>0</sup>		
		E037 .86879 <sup>0</sup>		
3	6A	S01 . 36499 <sup>0</sup>	Hot spot	
		E037 .86908 <sup>0</sup>		
	6B	S01 . 36499 <sup>0</sup>		
		E037 .86908 <sup>0</sup>		
	6C	S01 . 36507 <sup>0</sup>		
		E037 .86880 <sup>0</sup>		
4	7A	S01 . 36687 <sup>0</sup>	At the bridge	
		E037 .869960		

	7B	S01 . 36684 <sup>0</sup>	
		E037 .86981 <sup>0</sup>	
	7C	S01 . 36686 <sup>0</sup>	
		E037 .86962 <sup>0</sup>	
5	8A	S01 . 367960	
		E037 .86930 <sup>0</sup>	
	8B	S01 . 36782 <sup>0</sup>	
		E037 .86917 <sup>0</sup>	
	8C	S01 . 36771 <sup>0</sup>	
		E037 .86904 <sup>0</sup>	
6	9a	S01 . 29868 <sup>0</sup>	Altitude 1141
		E037 .94273 <sup>0</sup>	
	9b	S01 . 29878 <sup>0</sup>	Altitude 1143
		E037 .94276 <sup>0</sup>	
7	10	S01 . 29901 <sup>0</sup>	Altitude 1139
		E037 .94258 <sup>0</sup>	
	11	S01 . 29880 <sup>0</sup>	Altitude 1137
		E037 .94109 <sup>0</sup>	

## Sample collection sites along Tiva River



## Summary of sample collection sites

### First visit

Sample	Range	Location
A	A1 – A21	Downstream on lower side of bridge 1
B	B1 – B19	Downstream on upper side of bridge 1
C	C1 –C10 C11- C18	Upstream on upper side of bridge 3 Upstream on lower side of bridge 3
<b>Total</b>	<b>58</b>	

**Appendix 2:** Photograph of black sands found downstream



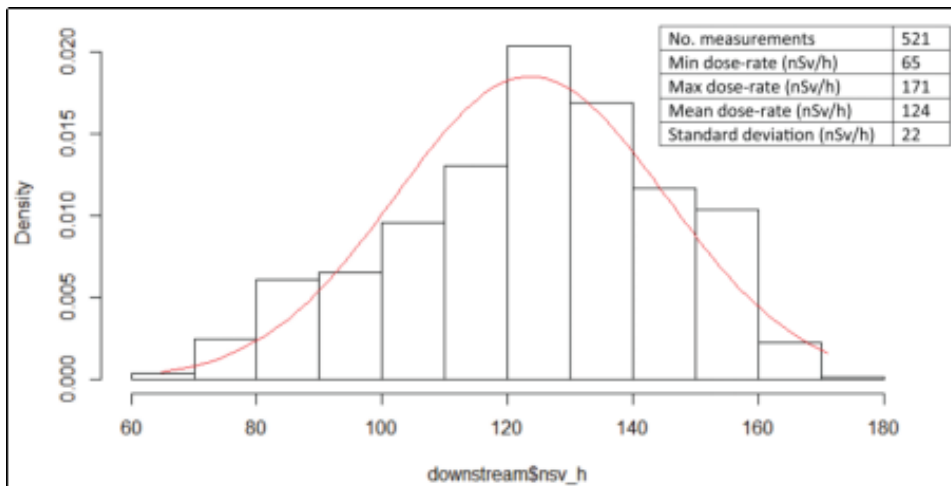
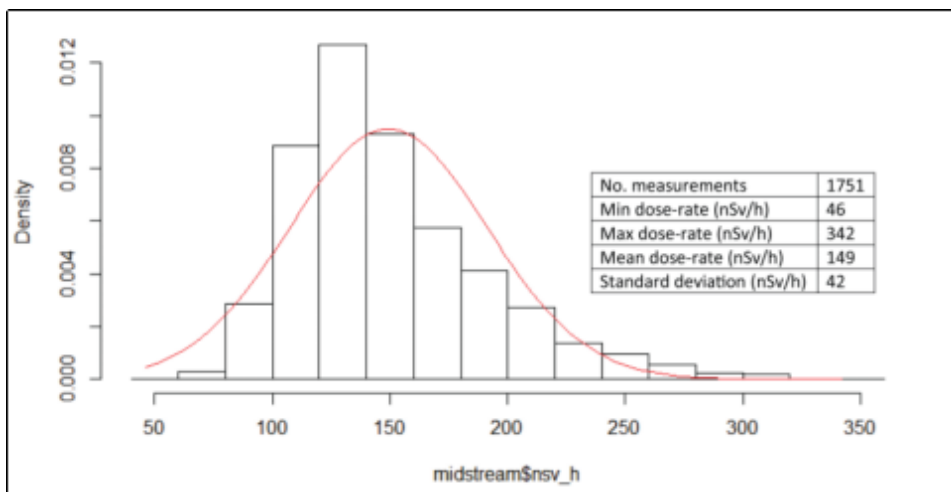
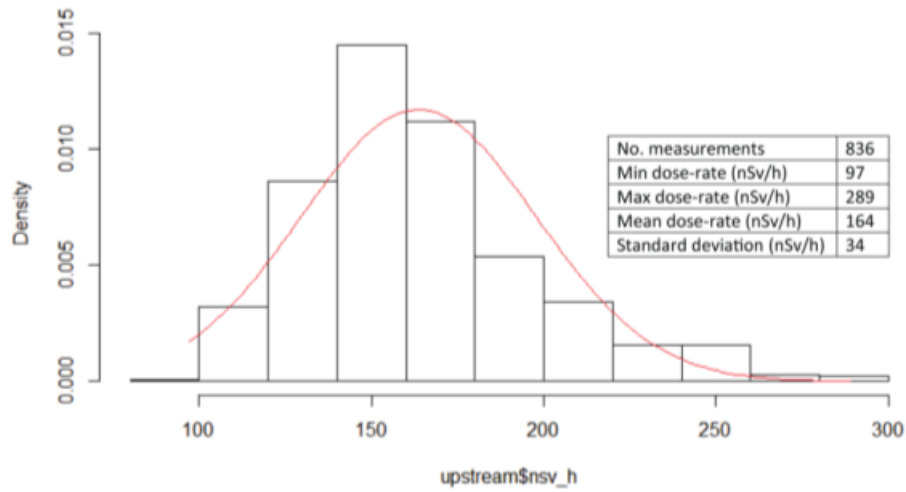
Fig. A.1 A pen magnet used to attract the black sands along the river channel.

**Appendix 3: Table A.1 results of activity concentrations along the chosen sites**

Lower downstream				Upper downstream				Upstream				Midstream			
samples	U-232	Th-238	K-40	samples	U-232	Th-238	K-40	samples	U-232	Th-238	K-40	Samples	U-232	Th-238	K-40
A1	32	51	497	B1	25	36	631	C1	23	32	562	4A	34	ND	ND
A2	27	47	477	B2	29	51	515	C2	19	33	576	4B	18	14	88
A5	29	42	418	B3	25	39	565	C3	24	38	551	4C	28	9	751
A7	27	39	389	B4	24	38	575	C4	17	32	574	5A	13	8	672
A9	22	30	659	B5	22	32	549	C5	22	28	601	5B	4	13	920
A10	28	34	634	B6	12	14	125	C6	14	22	583	5C	3	6	759
A11	27	37	598	B7	25	47	456	C7	18	25	596	6A	48	21	913
A12	30	23	459	B8	25	44	543	C8	14	21	646	6B	15	2	731
A13	19	21	640	B9	14	19	569	C9	18	27	597	6C	13	4	413
A14	25	45	604	B10	23	32	628	C10	24	30	589	7A	20	15	487
A15	27	39	612	B11	21	46	338	C11	14	29	564	7B	3	ND	872
A16	26	53	575	B12	38	70	471	C12	15	30	581	7C	11	6	681
A17	29	47	605	B13	10	12	718	C13	29	22	598	8A	7	7	686
A18	19	28	708	B14	19	40	442	C14	21	33	623	8B	13	6	829
A19	80	158	572	B15	24	39	564	C15	12	51	544	8C	9	10	777
Mean	30	46	563	B16	16	33	575	C16	31	43	634	9A	41	22	979
				B17	23	36	500	C17	13	18	555	9B	11	8	817
				B18	24	36	652	C18	23	38	537	10	8	ND	527
				B19	33	53	762	Mean	20	31	584	11	7	8	440
				Mean	23	38	536					HS02	6	8	430
												HS03	9	ND	752
												Mean	15.3	9.8	676.2



### Appendix 4: Histograms showing dose rate distribution in the three sites



## Appendix 5: Raw EDXRF measurement results for the elemental concentrations

**Table A2: Elemental concentrations from samples collected from Kauwi bridge (Upstream)**

	K	Ca	Ti	Mn	Fe	Ni	Ca	Zn	Rb	Sr	Y	Zr	Pb
CS1	21300±600	8817±284	2640±9	518±53	25300±200	334±11	287±7	BDL	52±9	716±29	BDL	110±7	15±2
CS2	15900±200	7273±438	3968±129	380±9	21600±600	310±1	277±22	31BDL	44±1	715±3	BDL	150±23	23±2
CS3	17300±600	5885±337	2306±115	387±0	18100±100	319±2	283±8	BDL	40±1	643±3	BDL	89±3	17±2
CS4	18500±500	11100±0	8317±46	469±0	32200±1300	351±13	305±11	40±3	44±2	810±24	BDL	256±22	18±2
CS5	14900±300	7423±842	7692±18	507±27	37000±300	332±10	283±0	33±2	32±3	622±7	BDL	238±0	22±1
CS6	24800±100	6570±508	4892±1	549±36	33500±800	377±23	316±13	BDL	56±3	729±39	11±1	172±11	BDL
CS7	13400±600	4180±246	3355±72	370±36	23800±1300	324±27	280±8	BDL	34±0	504±4	BDL	185±34	13±3
CS8	20600±1100	7930±156	4056±200	389±2	23200±0	325±10	259±3	BDL	46±0	755±6	BDL	173±12	20±4
CS9	19900±2300	7245±194	4983±98	639±2	29450±1250	357±6	314±3	BDL	47±3	738±11	BDL	216±13	19±3

CS10	19400±500	7893±86	5084±83	403±1	27200±500	317±11	261±8	BDL	45±3	644±16	BDL	179±2	22±2
CS11	28100±600	8399±198	5337±197	492±16	34300±200	352±37	301±1	36±0	52±1	666±12	BDL	175±7	18±6
CS12	15800±100	5174±336	3904±650	367±60	27100±600	339±23	281±22	BDL	46±2	632±6	BDL	205±16	16±0
CS13	19700±100	9100±400	7677±84	519±66	35000±300	358±4	309±4	40±1	42±1	679±25	12±1	293±10	14±1
CS14	18900±1000	6172±614	4524±99	461±5	30900±200	357±3	296±2	BDL	54±2	684±1	BDL	257±1	19±1
CS15	23200±1200	6458±239	6943±464	578±7	40600±600	320±5	296±0	BDL	56±6	667±2	BDL	409±43	14±2
CS16	17500±800	6490±409	2803±17	333±2	17800±100	335±8	277±4	BDL	38±1	651±3	BDL	98±5	16±2
CS17	20500±400	7194±261	3691±55	402±30	22500±400	331±2	272±3	BDL	52±1	783±17	10±0	148±13	16±1
CS18	17800±600	6934±8	4426±204	407±8	25700±700	344±0	286±1	BDL	49±1	719±1	10±0	188±24	15±2

BDL is below detection limit

**Table A3: Elemental concentrations from samples collected from Tanganyika (Midstream)**

	K	Ca	Ti	Mn	Fe	Ni	Ca	Zn	Rb	Sr	Y	Zr	Pb
4B	11600±500	8425±568	9786±759	408±10	26000±2400	265±6	257±18	47±2	22±0	562±57	BDL	1307±96	16±3
4C	8526±492	9062±72	9907±793	379±26	22400±600	243±8	225±7	BDL	18±1	515±10	BDL	705±12	16±4
5A	7133±806	6696±383	6660±510	267±33	17500±800	219±12	196±6	BDL	24±1	532±28	BDL	956±24	14±2
5B	11841±1959	8301±411	5071±840	277±47	13700±2100	198±8	195±1	BDL	26±1	527±35	BDL	350±189	12±0
5C	4694±144	7388±130	20200±1600	590±31	47600±2000	247±6	215±3	40±1	BDL	351±14	14±1	1560±124	17±0
6A	12800±700	6743±780	5212±557	390±11	15900±400	259±4	256±4	38±1	30±0	417±9	BDL	744±36	21±2
6B	3353±471	4607±480	30800±4400	782±152	70300±11400	269±6	278±2	69±4	BDL	286±5	29±1	4363±140	22±2
6C	3407±119	6846±134	46900±6900	1131±59	104900±6200	319±6	307±19	88±3	BDL	220±5	30±4	4501±153	21±1
7A	4001±399	6347±201	30800±2000	729±48	71100±3900	269±17	255±5	62±3	BDL	291±12	27±3	3584±522	19±2
7B	10200±236	8253±31	5683±95	294±6	14700±0	239±10	203±1	31±1	24±1	580±26	BDL	234±30	17±0
7C	5706±639	7575±1348	26500±500	684±6	57400±3000	278±16	281±12	64±2	16±1	428±16	18±3	1786±195	11±0
8A	4957±154	5549±283	8847±968	300±15	21400±1500	183±8	195±11	BDL	18±1	465±28	BDL	564±84	13±1
8C	14900±200	11800±0	20600±2100	608±50	48000±6300	301±41	274±22	48±5	26±0	522±63	12±1	1303±146	16±0
9A	10242±558	5461±459	4358±160	314±0	16750±350	268±8	235±1	34±0	41±4	423±9	BDL	613±31	20±5
9B	13100±800	5951±620	3596±103	256±5	12300±100	218±5	217±3	BDL	31±3	418±5	BDL	578±10	20±0
9C	4362±316	6415±369	17600±3600	566±20	41900±4500	243±4	238±2	37±1	19±1	497±48	19±1	1721±86	17±2
9A	11500±100	8563±345	5610±18	328±5	16700±300	240±6	230±0	BDL	30±0	592±5	BDL	502±38	18±2
HSO4	11500±100	8563±345	5610±18	328±5	16700±300	240±6	230±0	BDL	30±0	592±5	BDL	502±38	18±2
HSO2	12900±2700	11400±1703	42700±5500	1225±133	93600±7800	334±21	291±23	96±4	23±1	525±1	18±2	2132±25	16±1
HSO3	11400±500	11600±200	24200±1200	718±29	56400±0	295±25	267±4	64±2	18±1	422±3	18±5	1970±108	17±4
L1	15800±2000	9522±397	22100±500	678±8	52700±2900	260±23	250±15	50±3	27±0	534±17	11±1	1324±95	21±1
L2	7133±194	5359±30	5537±482	504±13	20800±600	245±12	209±19	BDL	29±1	382±13	BDL	573±15	23±1

BDL is below detection limit

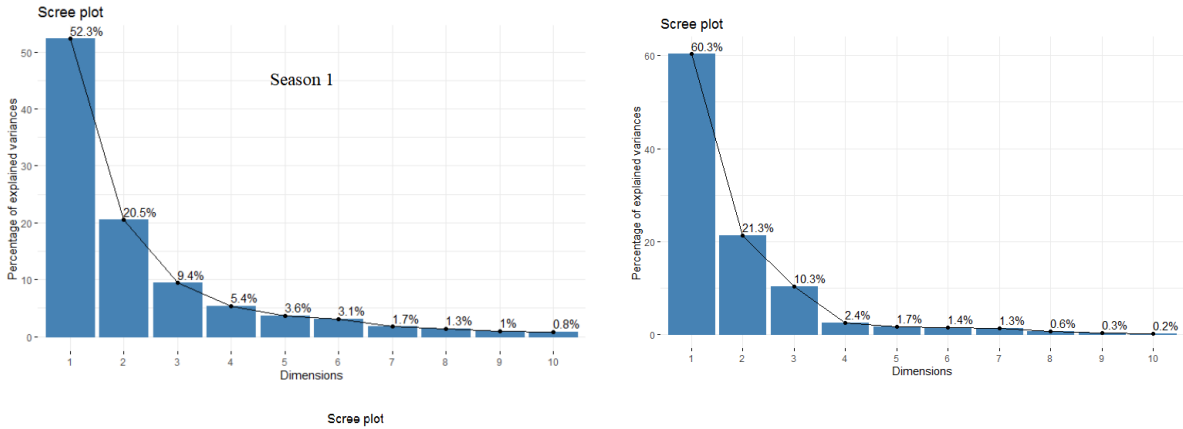
AS12	17400±900	8800±700	18400±800	949±33	75300±900	379±21	327±8	63±6	35±0	567±6	15±1	452±3	19±3
------	-----------	----------	-----------	--------	-----------	--------	-------	------	------	-------	------	-------	------

**Table A4: Elemental concentrations from samples collected from Tanganyika (Midstream)**

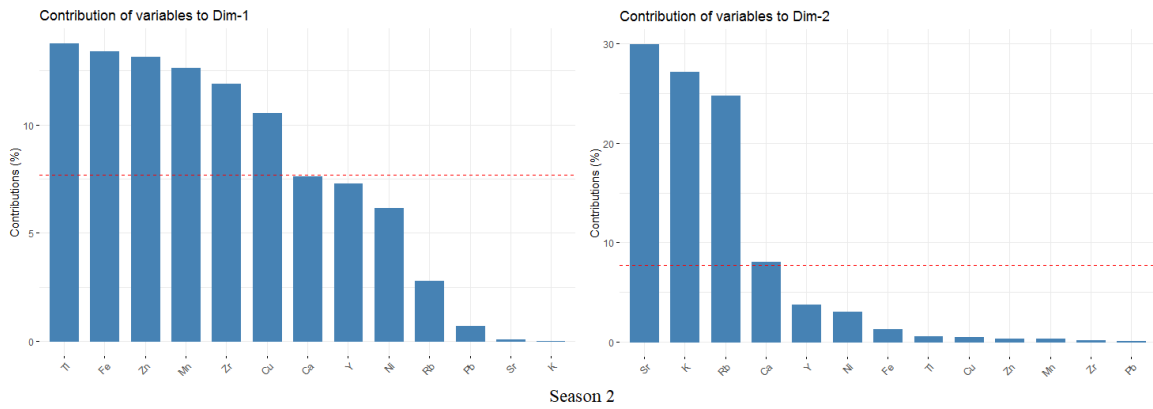
	K	Ca	Ti	Mn	Fe	Ni	Ca	Zn	Rb	Sr	Y	Zr	Pb
AS1	17300±200	11200±0	22300±100	873±33	76800±600	401±26	362±0	62±4	38±2	755±8	19±0	619±12	20±2
AS2	21000±1000	7810±150	7128±237	486±23	34000±600	337±10	284±2	36±2	45±4	747±12	BDL	241±7	23±0
AS3	16900±1500	9385±514	18700±0	690±21	60700±500	348±10	314±10	48±1	35±1	687±9	12±0	481±6	18±3
AS4	17800±300	6794±162	3344±243	472±17	28900±500	320±3	270±3	BDL	47±1	744±11	11±0	194±7	29±7
AS5	17000±500	9154±63	14600±100	704±31	54300±500	351±19	306±10	51±6	32±0	614±4	BDL	337±6	13±1
AS6	20600±1100	6755±236	5972±481	588±5	39500±800	299±4	295±9	33±2	44±0	734±4	BDL	221±16	19±1
AS7	18200±200	8505±245	19000±200	826±56	74000±1400	339±4	326±4	54±4	29±1	553±8	12±1	407±2	15±3
AS8	15200±800	7529±894	14900±1000	666±57	56300±2700	329±0	306±6	51±1	31±3	559±22	BDL	365±8	22±3
AS9	18800±2500	8383±1178	4620±121	512±0	31700±500	323±4	304±19	BDL	40±2	678±11	11±1	183±4	17±2
AS10	16400±400	8600±300	7584±375	466±23	31300±800	289±8	270±11	34±1	47±2	851±28	13±0	478±19	20±0
AS11	20200±500	9800±500	13400±200	739±13	54900±600	338±10	310±7	47±2	46±0	734±19	13±1	389±2	25±1

AS13	21500±7000	7931±1596	3687±436	595±84	31800±600	346±5	303±8	BDL	42±2	739±6	BDL	148±20	17±1
AS14	18600±600	8393±100	12100±100	601±10	49400±1400	331±12	305±6	47±11	37±1	720±9	16±1	338±4	20±3
AS15	20100±1300	11400±0	15300±100	662±1	54200±600	374±24	321±7	51±9	35±1	755±4	14±1	553±14	13±1
AS16	23100±400	9171±183	17600±100	754±12	63900±200	367±1	326±1	60±3	45±0	793±1	14±0	409±5	17±0
AS17	22300±2900	9204±570	8831±51	502±26	34800±700	349±26	313±9	44±6	40±2	773±4	11±1	315±12	19±1
AS18	23600±700	6435±81	5377±286	537±58	30300±1400	314±32	260±18	BDL	44±3	818±10	12±0	198±7	17±1
AS19	25100±600	28700±1000	99800±1100	2302±61	199000±1000	502±0	430±12	155±10	26±2	660±33	33±3	1820±2	29±7
AS20	22800±700	25200±800	122600±4100	2577±30	247700±9700	500±6	465±1	209±7	26±0	556±10	41±4	2514±110	27±9
AS21	24100±100	12000±100	18000±100	720±6	59400±400	376±3	346±3	58±1	43±0	836±7	16±0	684±5	14±0
BS1	12900±1000	7492±486	8947±277	510±24	37000±400	275±28	266±19	41±10	27±0	532±3	BDL	288±16	20±3
BS2	17300±200	9221±1079	17100±300	732±18	64500±100	344±18	307±6	53±1	36±1	676±15	13±2	552±9	14±0
BS3	18700±2300	8699±479	10800±500	612±57	48300±400	345±15	311±5	40±6	37±3	672±4	14±1	331±5	BDL
BS4	16800±300	7748±573	10500±500	595±19	46200±1100	362±2	315±4	43±3	38±2	689±17	11±0	356±20	19±2
BS5	20600±200	6968±400	8179±234	578±24	42400±2000	325±27	285±23	33±2	41±2	690±26	12±0	283±2	14±1
BS6	13500±400	7399±206	15000±0	793±18	67700±1500	355±16	345±10	47±11	29±0	548±11	14±2	372±16	16±0
BS7	18800±100	9147±360	20100±100	904±3	76800±600	354±17	307±4	64±2	40±1	664±10	17±2	519±12	13±1
BS8	21800±600	9526±874	11900±200	708±13	56300±200	352±15	301±32	38±2	43±0	715±21	13±1	321±4	18±2
BS9	18900±600	6972±157	4656±356	461±20	27500±100	326±2	276±11	BDL	45±3	786±13	BDL	205±9	22±1
BS10	15600±800	6128±361	6141±61	515±33	33300±100	340±3	302±5	41±4	41±2	709±9	BDL	237±3	29±1
BS11	14600±1600	7954±125	15600±100	765±9	64000±100	370±13	334±4	64±2	30±4	562±17	12±0	420±1	21±1
BS12	19800±1400	12700±1300	32300±800	1127±91	98300±500	366±16	340±13	84±16	32±1	647±0	15±1	774±7	16±1
BS13	14900±1700	9833±418	14700±800	689±30	58800±1100	341±5	348±5	44±3	31±1	560±7	11±0	521±5	15±1
BS14	25000±1300	11300±400	8700±51	313±2	39800±600	340±5	309±2	44±3	23±1	1184±30	20±0	177±15	23±1
BS15	21100±900	9600±900	13500±200	824±35	55400±800	360±12	332±19	43±4	41±0	739±31	12±1	414±7	12±0
BS16	16900±1100	6180±91	9105±60	652±24	43400±300	342±4	300±2	36±2	37±2	688±34	BDL	291±2	14±4
BS17	14250±1450	6763±334	11050±250	698±39	53500±2600	306±10	292±1	46±2	36±3	621±19	16±0	390±11	18±2
BS18	20400±200	8288±58	6838±8	577±18	36600±200	329±15	289±5	38±2	47±1	897±0	12±1	293±10	15±2
BS19	20600±0	10400±0	15600±500	652±54	51700±600	346±1	317±2	49±5	42±0	816±3	BDL	484±9	15±1

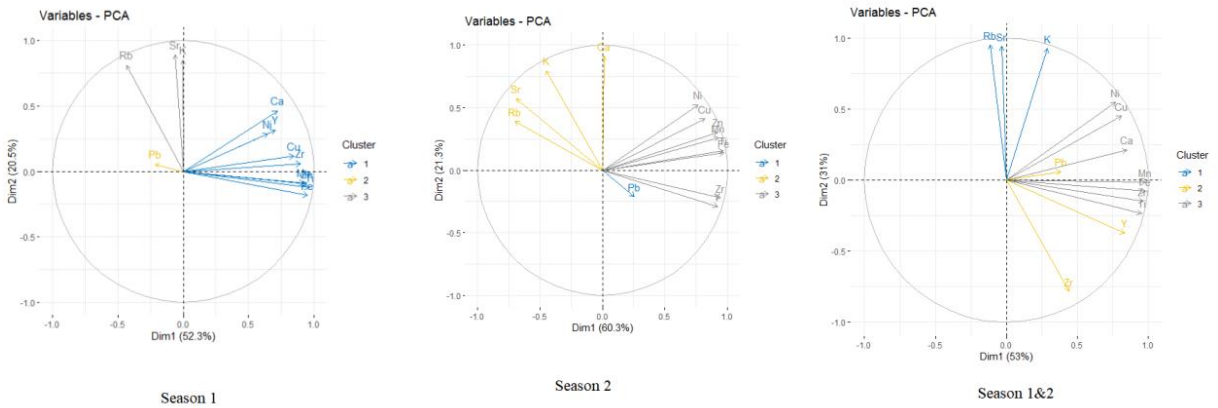
## Appendix 6: Additional results for PCA



(a) PCA scores plot



(b) Contributions of elements to PC1 and PC2



(c) Loadings for PC1 and PC2

## Appendix 7: Spatial distribution of Fe, Ti and Zn

